

Voltage Transients in the Field Winding of Salient Pole Wound Synchronous Machines

Implications from fast switching power electronics

Roberto Felicetti



UPPSALA
UNIVERSITET

Licentiate thesis to be presented at Uppsala University, Högssalen 10132, Ångströmlaboratoriet, Lägerhyddsvägen 1, Uppsala, Friday, 12 March 2021 at 10:00. The examination will be conducted in English.

Abstract

Felicetti, R. 2021: Voltage Transients in the Field Winding of Salient Pole Wound Synchronous Machines: Implications from fast switching power electronics. 91 pp. Uppsala.

Wound Field Synchronous Generators provide more than 95% of the electricity need worldwide. Their primacy in electricity production is due to ease of voltage regulation, performed by simply adjusting the direct current intensity in their rotor winding. Nevertheless, the rapid progress of power electronics devices enables new possibilities for alternating current add-ins in a more than a century long DC dominated technology. Damping the rotor oscillations with less energy loss than before, reducing the wear of the bearings by actively compensating for the mechanic unbalance of the rotating parts, speeding up the generator with no need for additional means, these are just few of the new applications which imply partial or total alternated current supplying of the rotor winding.

This thesis explores what happens in a winding traditionally designed for the direct current supply when an alternated current is injected into it by an inverter. The research focuses on wound field salient pole synchronous machines and investigates the changes in the field winding parameters under AC conditions. Particular attention is dedicated to the potentially harmful voltage surges and voltage gradients triggered by voltage-edges with large slew rate. For this study a wide frequency band simplified electromagnetic model of the field winding has been carried out, experimentally determined and validated. Within the specific application of the fast field current control, the research provides some references for the design of the rotor magnetic circuit and of the field winding. Finally the coordination between the power electronics and the field winding properties is addressed, when the current control is done by means of a long cable or busbars, in order to prevent or reduce the ringing.

Keywords: Apparent resistance, cable modeling, current control, transmission line model, eddy currents, field winding, frequency analysis response, Fourier Transform, impedance mismatch, main inductance, overvoltage, parasitic capacitance, partial discharge, quality factor, ringing, slew rate, stray inductance, voltage gradient, winding resonance frequency.

Roberto Felicetti, Uppsala University, Department of Electrical Engineering,
Box 65, SE-751 03 Uppsala, Sweden.

© Roberto Felicetti 2021

urn:nbn:se:uu:diva-434652 (<http://urn.kb.se/resolve?urn=urn:nbn:se:uu:diva-434652>)

To Pier Antonio Abetti
(Florence, February 7th 1921)

List of Papers

This thesis is based on the following papers, which are referred to in the text by their Roman numerals.

- I Felicetti, R., Abrahamsson, C.J.D., Lundin, U. (2019) Experimentally validated model of a fast switched salient pole rotor winding, *IEEE Workshop on Electrical Machines Design, Control and Diagnosis (WEMDCD)*, Athens, pp. 150-156.
- II Felicetti, R., Abrahamsson, C.J.D., Lundin, U. (2020) The influence of eddy currents on the excitation winding impedance of solid and laminated salient pole synchronous machines, *Electr Eng*, 102, pp. 2553–2566.
- III Felicetti, R., Abrahamsson, C.J.D., Lundin, U. (2021) An experimentally determined field winding model with frequency dependent parameters. The paper has been accepted for publication in the journal *IET Electr. Power Appl.*
- IV Felicetti, R., Perez Loya, J.J., Lundin, U. (2021) Simulation of rapid front edges related voltage surges in highly inductive windings with frequency dependent parameters. Manuscript.

Reprints were made with permission from the respective publishers.

Contents

1.	Introduction	13
1.1.	Background	13
1.2.	Challenges and research questions	14
1.3.	Thesis outline	20
2.	Theoretical background	21
2.1.	Eddy currents effect on the winding resistance and inductance	21
2.2.	The distributed parameters model of the winding and the travelling waves	26
2.3.	The distributed parameters model in the frequency domain	28
2.4.	The importance of the modal dispersion	32
2.5.	A frequency dependent winding model	34
3.	Methods	37
3.1.	The analysis of the winding transfer function	37
3.2.	The experimental determination of the parameters	39
3.2.1.	<i>The parasitic capacitances of the winding</i>	40
3.2.2.	<i>The parallel resistance of the winding</i>	42
3.2.3.	<i>The inductance of the winding</i>	44
3.3.	The simulation in the time-domain	45
4.	Results and Discussion	49
4.1.	The parameters of the winding	49
4.1.1.	<i>The winding capacitances</i>	50
4.1.2.	<i>The winding resistance</i>	53
4.1.3.	<i>The winding inductance</i>	54
4.2.	The frequency response of the winding	58
4.3.	The time domain simulation	59
4.3.1.	<i>The steady state simulation</i>	60
4.3.2.	<i>The subcritical behavior</i>	61
4.3.3.	<i>The supercritical behavior</i>	62
5.	Main outcomes of this work	67
5.1.	Relevant parameters for modeling the field winding and the feeder	67
5.1.1.	<i>The field winding parameters</i>	67
5.1.2.	<i>The feeder parameters</i>	69

5.2.	Measures for reducing the electric stress.....	70
5.2.1.	<i>The field winding design</i>	70
5.2.2.	<i>The reduction of the voltage slew rate</i>	72
6.	Conclusions	77
7.	Future work.....	79
8.	Summary of papers.....	80
9.	Svensk sammanfattning	82
10.	Acknowledgments	83
	References.....	84
	Appendices.....	87
A.1	Travelling waves equations	87
A.2	The propagation speed.....	88
A.3	Poles of the voltage transfer function	89
A.4	The winding voltage gradients	90
A.5	The natural frequencies and the inductance law.....	90

Abbreviations and nomenclature

Abbreviation	Description
AC	Alternating Current
DC	Direct Current
ES	Excitation System
FRA	Frequency Response Analysis
FT	Fourier Transform
HESM	Hybrid Excitation Synchronous Motor
Hi-Pot	High Potential Test
IGBT	Insulated Gate Bipolar Transistor
MOSFET	Metal Oxide Silicon Field Effect Transistor
MTLM	Multi-conductor TLM
ODE	Ordinary Differential Equation
PD	Partial Discharge
PE	Power Electronics
PMSM	Permanent Magnet Synchronous Machine
STLM	Single TLM
TF	Transfer Function
TLM	Transmission Line Model
UMPC	Unbalanced Magnetic Pull Compensation
VSC	Voltage Source Converter
WFSM	Wound Field Synchronous Machine

Symbol¹	SI Unit	Description
a	m	Winding length
a_f	m	Feeder length
b	m	Depth of the iron lamination
B	T	Magnetic flux density
c	Fm ⁻¹	Winding specific capacitance
C_f	F	Feeder capacitance
C_g	F	Capacitance to ground of the machine frame
C_p	F	Winding capacitance to the machine frame

¹ The symbols used in the comprehensive summary might differ from the notation used in the published papers.

Symbol¹	SI Unit	Description
C_s	F	Winding series capacitance
C_∞	F	Supercritical capacitance of the winding
\bar{F}_x	-	Voltage transfer function
\mathfrak{F}	-	Fourier Transform
\mathfrak{F}^{-1}	-	Fourier Inverse-Transform
g	Sm^{-1}	Specific conductance of the winding insulation
H	Am^{-1}	Magnetic field
$i(x, t)$	A	Winding instantaneous current at the position x
$i_l(x, t)$	A	Winding conduction current at the position x
$i_k(x, t)$	A	Winding displacement current at the position x
J	Am^{-2}	Current density
k	$\text{F}^{-1}\text{m}^{-1}$	Winding specific elastance
\bar{K}, \mathbf{K}	m^{-1}	Winding propagation constant
L	H	Inductance
L_{DC}	H	Inductance value for the DC-current
L_F	H	Low-pass filter inductance
l	Hm^{-1}	Winding specific inductance
l_e	Hm^{-1}	Specific inductance of the eddy current path
L_p	H	Parallel inductance of the field winding
l_e	Hm^{-1}	Specific inductance of the eddy current path
N	-	Number of turns per pole
Q	-	Winding quality factor
r_e	$\Omega \text{ m}^{-1}$	Specific resistance of the eddy current path
r_p	$\Omega \text{ m}^{-1}$	Winding specific parallel resistance
r_w	$\Omega \text{ m}^{-1}$	Specific wire resistance of the winding
R_p	Ω	Parallel resistance of the field winding
\mathcal{R}	H^{-1}	Reluctance
s	m	Lamination thickness
s	s^{-1}	Complex frequency
u	ms^{-1}	Wave propagation speed
$v(x, t)$	V	Winding instantaneous voltage at the position x
w	m	Thickness of the iron lamination
x	m	Measurement position along the winding
y	Sm^{-1}	Line model specific admittance
z	$\Omega \text{ m}^{-1}$	Line model specific impedance
\bar{Z}_0	Ω	Characteristic impedance

Symbol¹	SI Unit	Description
β	m^{-1}	Wave number
δ	m	Penetration depth
ε	Fm^{-1}	Dielectric permittivity
ε_r	-	Relative dielectric permittivity
ε_0	Fm^{-1}	Dielectric permittivity of vacuum
ζ	-	Winding damping factor
θ_e	A	Magneto motive force of the eddy currents
λ	m	Wave length
μ	Hm^{-1}	Magnetic permeability
μ_r	-	Relative magnetic permeability
μ_0	Hm^{-1}	Magnetic permeability of vacuum
ξ	-	Relative voltage peak position
τ	s	Rise time
Φ	Wb	Magnetic flux
χ	-	Relative rise time
ω	s^{-1}	Angular frequency
ω_c	s^{-1}	Critical angular frequency of the field winding
ω_m	s^{-1}	Natural angular frequency of the field winding
$\omega_{r,m}$	s^{-1}	Resonance angular frequency of the field winding

1. Introduction

1.1. Background

Synchronous generators cover more than 95% of the electricity need worldwide [1]. The reason for the use of the Wound Field Synchronous Machine (WFSM) in the electricity production is the ease of voltage regulation, performed by simply adjusting the direct current (DC) intensity in the rotor winding. Nevertheless, the rapid progress of power electronics (PE) devices enables new possibilities for alternating current (AC) add-ins in a more than a century long DC dominated technology. Damping the rotor oscillations with less energy loss than before, reducing the wear of the bearings by actively compensating for the mechanic unbalance of the rotating parts, speeding up the generator with no need for additional means. These are just few of the new applications which imply partial or total AC supplying of the rotor winding. But, what does happen in a winding designed for DC-current when an AC one flows through it? What does an intermittent supplying voltage provokes in a highly inductive winding, when the Power Electronics Switches perform the field current control? This thesis addresses such questions from a theoretical and experimental point of view in solid salient pole WFSM. Its main outcome is a Single Transmission Line Model (STLM) suitable for studying and reproducing fast turn-to-turn and turn-to-ground voltage transients in the excitation winding. The model is presented together with the experimental methods and setups to be used on the test synchronous machine (SM), in order to determine its main frequency dependent and non-dependent parameters. Besides, some simple yet useful references are given for coordinating the power electronics control and the winding design, so to prevent harmful voltage overshoots and voltage gradients in the field winding.

1.2. Challenges and research questions

The main topologies of WFSM produced nowadays are essentially two: the round-rotor and salient-pole type. The first one is used in large and fast synchronous generators (pole pair $p \leq 2$) whereas the other one dominates all remaining applications. Although both topologies are older than a century [2], all significant improvements achieved since then, in the insulation technique as well as in the cooling strategies, do not have changed their structure essentially [3]. On the contrary, the excitation system has undergone a radical change after the '50s of the last century thanks to the progresses of the solid state electronics [4]. Diodes and thyristors have made it possible to replace the electromechanical rotating DC exciter (Figure 1) with an AC supplied Excitation System (ES).

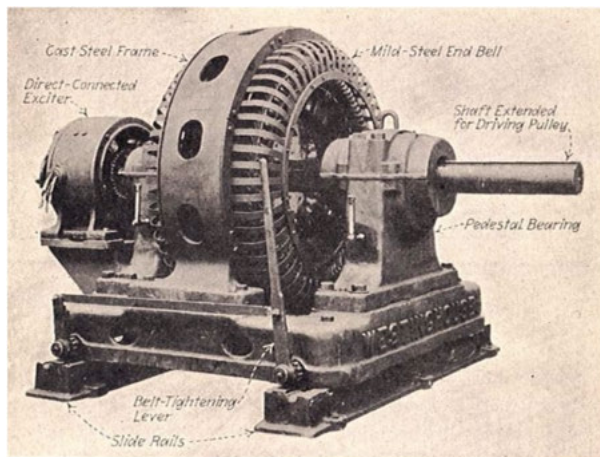


FIGURE 1 – A Westinghouse Type C belt-driven Synchronous motor with direct – connected exciter (figure adapted from [5]).

Nowadays, diodes and thyristors still play a major role in the three main categories of ESS, static-(Figure 2), brushless- and embedded-ones.

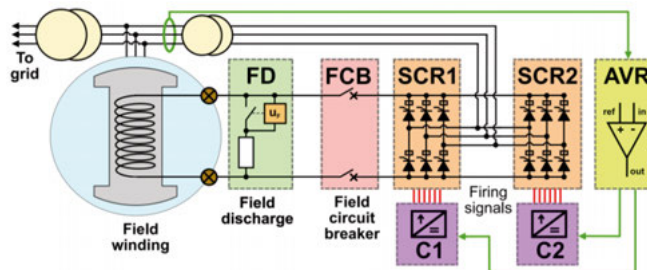


FIGURE 2 – Components of a static excitation system (figure from [4]).

However, in the first decade of the new century, the use of IGBTs in the ES topologies has become more and more frequent. In the static ES for example, IGBT based voltage-boosters and buck-boosters have been introduced between the Voltage Source Converter (VSC) and the field winding, in order to increase the positive and negative ceiling voltages respectively (Figure 3).

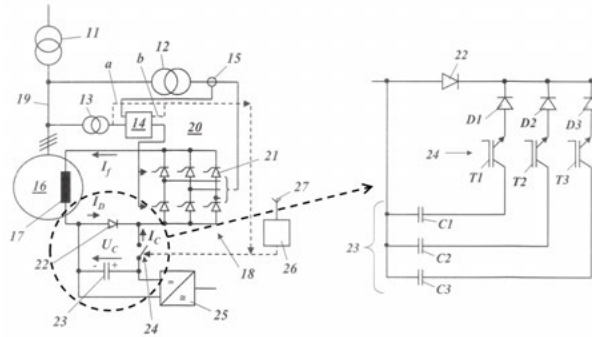


FIGURE 3 – A voltage booster using IGBTs (figure adapted from [6]).

In some other cases, a double quadrant H-bridge chopper made of IGBTs has been used for adjusting the excitation voltage (Figure 4).

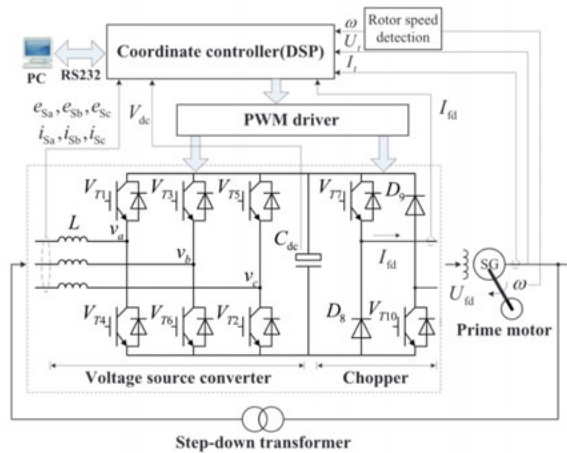


FIGURE 4 – A VCS using a back-end H-bridge chopper with IGBTs (figure from [7]).

The brushless ESs (Figure 5) have taken even more advantage from integrating IGBT-based choppers, which knowingly improve their dynamic performance.

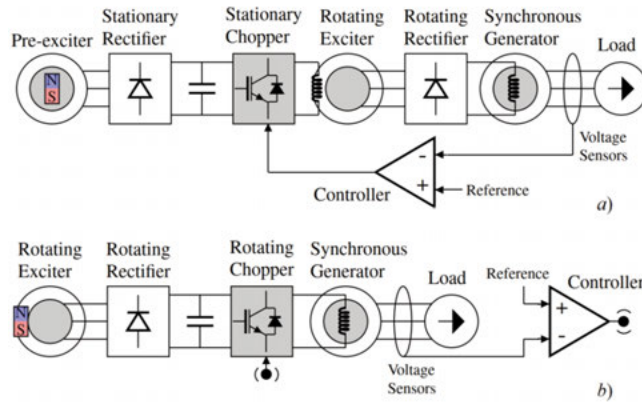


FIGURE 5 – Brushless ESs with IGBTs (figure adapted from [8]).

The IGBTs have found application also in the embedded ESs. In the example reproduced in Figure 6, the electromotive forces harvested by special auxiliary windings placed on the rotor are first rectified for setting the DC-link voltage. Then, the field current is controlled by switching the IGBTs in the Power Module.

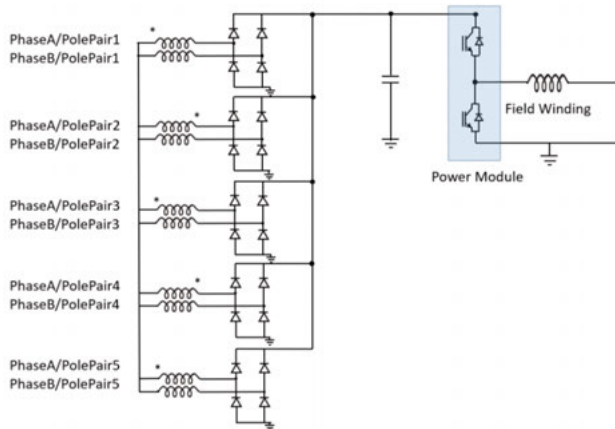


FIGURE 6 – Brushless ESs with IGBTs (figure adapted from [9]).

The AC current injection in the field winding is a novel technique aimed to achieve additional performances from a classical ES. The Unbalanced Magnetic Pull Compensation (UMPC) [10] for example uses the AC current injection in a split rotor field winding for compensating static and dynamic radial forces stressing the radial bearing of a synchronous machine. The concept proposed for the UMPC uses IGBTs and it is shown in Figure 7.

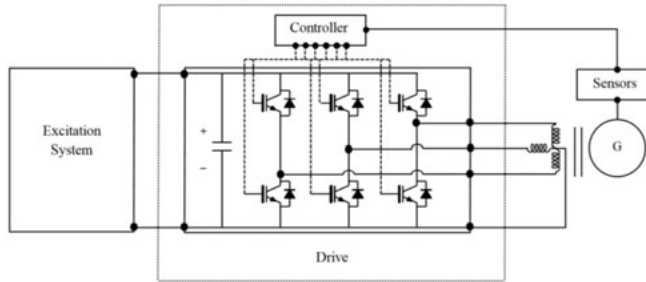


FIGURE 7 – Brushless ESs with IGBTs (figure adapted from [10]).

The almost sinusoidal AC-current injections, as well as the DC-current bias in the three rotor sectors, are obtained by sensing the current level in the different field winding portions and by updating the state of the switches accordingly. This concept, which also uses IGBT modules, has been successfully applied and tested to the ES of a 10 MVA, 600 rpm generation unit of the Swedish hydropower plant in Porjus.

The motor start by polarity inversion [11] is another example of AC-current injection in the field winding. It aims to produce the rotor start by synchronizing a pulsating steady-state magnetic field of the rotor with the rotating magnetic field of the armature. Figure 8a represents the four-quadrants H-bridge used for the experimentation of this starting technique on a 200 kVA, 500 rpm SM.

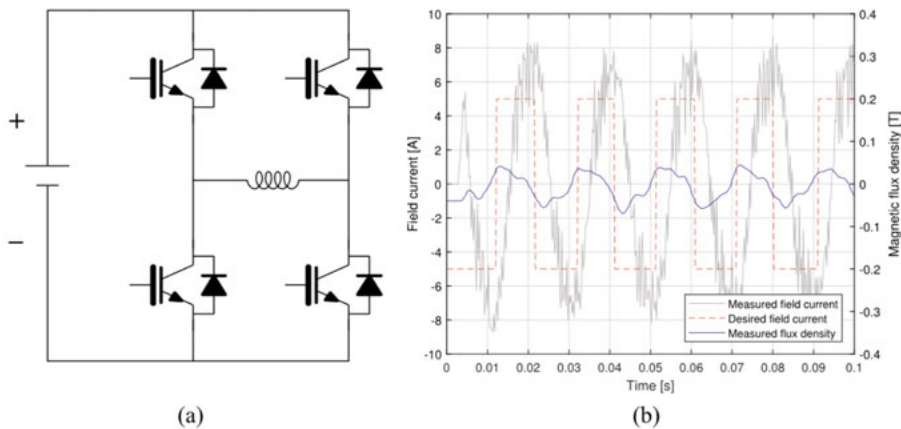


FIGURE 8 – The machine start by rotor polarity inversion: a) the driving H-bridge, b) the field current and the airgap field at stand still (figure adapted from [11]).

In this specific application of the current control, the use of IGBTs can be recognized.

Moving the attention away from the electricity production for a while, it is still possible to find further applications where the field cur-

rent is controlled by switches other than thyristors. In the electric propulsion for instance, the need for an effective flux-weakening in permanent magnet synchronous motor (PMSM), combined with the need for reducing the weight of the expensive rare-earths magnets, has awaked in the last decade the interest about hybrid excited synchronous motors (HESM) [12]. Some of these special PMSM (Figure 9) present a salient pole rotor structure embedding a traditional field winding.

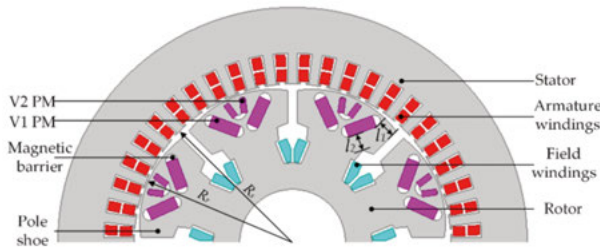


FIGURE 9 – Topology structure of hybrid excitation synchronous motor (HESM) (figure from [13]).

In this way, by controlling the demagnetizing actions of the armature Magneto Motive Force (MMF) on the d-axis and inverting the sense of the field current, the main flux established by the permanent magnets can be effectively opposed. This application, which envisages motor sizes up to hundreds of kilowatt, refers to field current and voltage ratings which are compatible with the usage of IGBTs. Moreover, in all the presented applications so far, if the field current and voltage are not as high as to forcibly require IGBTs, it is possible to make alternatively use of MOSFETs.

IGBTs and power MOSFETs are known to switch faster than thyristors [14]. *Therefore, the increasing application of faster switches to a traditionally consolidated thyristor-based technology naturally leads to the risk of triggering potentially harmful voltage surges and gradients into the rotor windings.* This kind of issue is already known with reference to the armature windings of AC-machines, where the application of IGBTs and MOSFETs represents the state of the art in the PE-drives [15]. Moreover, the introduction of SiC switches has recently addressed the interest to the voltage surges produced into AC-windings by very large voltage slew-rates [16-18]. Particularly sensitive to this issue are the low voltage windings. In fact, since the ageing of the insulation in low voltage windings is mainly thermally related, these are usually not designed for facing the risk of partial discharge [15]. In order to assess the electric stress produced on the insulation of low voltage three-phase machines by the switching of PE-drives, the standard IEC 60034-18-41

[19] considers two parameters: the relative intensity of the caused overvoltage (Overshoot Factor) and the rise time (Impulse Rise Time) of the voltage pulse applied to the winding. In Table 1, it is shown that short rise times are related to higher values of the overshoot factor and to an increasing severity of the produced electric stress.

TABLE 1 – Stress categories for insulation systems according to the standard IEC 60034-18-41 (table adapted from [15]).

Stress category	Overshoot Factor (p.u.)	Impulse Rise Time (μs)
A-Benign	$\text{OF} \leq 1.1$	$1 \leq t_r$
B-Moderate	$1.1 < \text{OF} \leq 1.5$	$0.3 \leq t_r < 1$
C-Severe	$1.5 < \text{OF} \leq 2.0$	$0.1 \leq t_r < 0.3$
D-Extreme	$2.0 < \text{OF} \leq 2.5$	$0.03 \leq t_r < 0.1$

The field winding is typically a low voltage winding, nonetheless it has remained so far excluded from this kind of considerations.

Standard overvoltage tests for the field winding insulation of WFSM already exist. The High-Potential test (Hi-Pot) for the excitation winding, which is described by the Standards IEC 60034-1 and IEEE C50.13, consists in stressing the field winding with a given AC voltage (50/60 Hz) for 1 minute. The test-voltage level depends on the rated excitation voltage, $V_{f,R}$: it corresponds to 10-times the field winding rated voltage and at least 1.5 kV, for $V_{f,R} < 500$ V; otherwise, 2-times the field winding rated voltage plus 4 kV. It is clear that the nature of the Hi-Pot test is very different from the kind of stress described by Table 1. In fact, the Hi-Pot-test is intense, persistent but it is related to sporadic failure events, which could potentially happen during the SM life-time. The electric stress produced by the fast switching of power electronic devices can be intense, persistent, but its main characteristic is to be repetitive. Besides, at the frequency of 50/60 Hz the voltage distribution along the field winding is linear whereas for very fast voltage fronts (which recall very high frequencies) it decays almost exponentially. In this last case (see paragraph 4.2), the specific voltage gradients at the terminals of the winding can be amplified up to 5÷10 times. So, the fact that the field winding passes the Hi-Pot test does not imply that it can withstand PD triggering voltage stresses, like the ones produced by repetitive fast voltage edges.

The work presented in this thesis has moved from the just outlined overview in order to accomplish three tasks essentially:

1. verifying if fast rising voltage edges can produce overvoltages and voltage gradients in the field winding, as well as these do in the armature winding of AC-machines;
2. identifying the parameters which influence the amplitude of the overvoltages and the strength of the voltage gradients in the field winding; and
3. considering possible measures for avoiding or mitigating overvoltages and voltage gradients in the field winding.

The research has been carried out by using an experimentally validated model for the field winding. The conception of the model, the delineation of its performances as well as the description of the experimental procedures necessary to characterize it, have represented the main part of this research work.

1.3. Thesis outline

In order to address the aforementioned tasks an initial phase of theoretical work has been required. It has helped to understand the physics behind the overvoltage phenomena in solenoid-like windings. The principal arguments faced during this activity are presented in a logical sequence in Chapter 2, which does not reflect the chronological order of their consideration. The background gained in that way has greatly helped in attaining a simple, yet complete, model. Moreover, it has shed light on how to better perform the experimental work. Chapter 3 is dedicated to the description of the used methods. All conceived setups and experimental procedures are presented and explained. The matter is addressed by following the determination of the field winding parameters, one by one. Chapter 4 outlines the obtained results, presenting them in two groups: the experimental work performed for characterizing the model (the model parameters) and the experimental work done for validating the model (the voltage simulations). The latter outcomes are the most important, since they fulfill the goals of the thesis and disclose the importance of the followed approach. In Chapter 5, the discussion about the results points first to what is relevant in the model and what is not. Thereafter, a summary of the most relevant measures is presented, which can prevent or mitigate the voltage stress in the field winding of a salient pole WFSM. Finally, Chapter 6 draws some conclusions while Chapter 7 outlines potential continuations and improvements of the work done.

2. Theoretical background

2.1. Eddy currents effect on the winding resistance and inductance

In considering the absorption of energy related to harmonic electromagnetic waves in ferromagnetic material W. Arkadiew [20] first recognized that the relationship between the flux density \bar{B} and the magnetic field \bar{H} has a complex nature

$$\bar{\mu} = \frac{\bar{B}}{\bar{H}} = \frac{B}{H} e^{-j\varphi} = \mu' - j\mu'' \quad (1)$$

The real part, μ' , of the complex permeability, $\bar{\mu}$, relates to the storage of magnetic energy in the matter, whereas the imaginary part, μ'' , takes into account the losses produced in the material by a variable magnetic field. The parameter μ'' summarizes the hysteresis-, eddy currents- and excess-losses and is responsible for the lagging of the flux density on the magnetic field.

Taking a portion of magnetic material with cross section, S , and length, l , crossed by a constant magnetic flux, $\bar{\Phi}$, from (1) occurs immediately the concepts of complex reluctance

$$\bar{\mathfrak{R}} = \frac{l}{\bar{\mu}S} = \frac{l}{\mu^2 S} \mu' + j \frac{l}{\mu^2 S} \mu'' = \frac{\bar{\mu}^* l}{\mu^2 S} \quad (2)$$

and complex inductance

$$\bar{L} = \frac{N^2}{\bar{\mathfrak{R}}} = N^2 \frac{S}{l} \mu' - jN^2 \frac{S}{l} \mu'' = L' - jL'' \quad (3)$$

where N is the number of turns of the coil linking the magnetic flux.

The voltage drop, \bar{V} , across the inductor having inductance, \bar{L} , produced by a current, \bar{I} , flowing through it, is

$$\bar{V} = j\omega\bar{L}\bar{I} = \omega L''\bar{I} + j\omega L'\bar{I} \quad (4)$$

At the right hand of (4), it can be noticed that the voltage drop, \bar{V} , has a component in phase with the current, which can be assimilated to a resistive voltage drop. In Figure 10a, the equivalent circuit of the inductor can be observed, where the resulting resistance, R , is equal to

$$R = \omega L'' \quad (5)$$

One effect of the presence of eddy currents in the magnetic circuit of an inductor, besides the effect of hysteresis and excess losses, is that of increasing the winding AC-resistance in the same way the skin effect or the proximity effect do.

In the transformer theory, the iron losses in general are taken into account by a resistance in parallel to the magnetizing inductance according to the circuit in Fig. 10b, where

$$L_p = L' \left[1 + \left(\frac{L''}{L'} \right)^2 \right] \quad (6)$$

and

$$R_p = \omega L'' \left[1 + \left(\frac{L'}{L''} \right)^2 \right]. \quad (7)$$

Therefore, by changing the arrangement of the equivalent circuit by means of equations (6) and (7), it can be observed that one effect of the eddy currents is that of establishing an AC resistance in parallel to the source of a self-induced electromotive force.

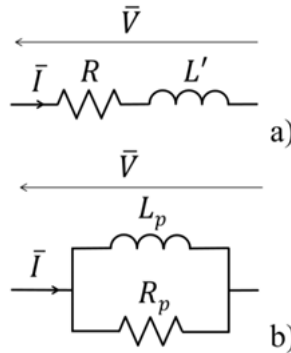


FIGURE 10 – The electric models for an inductance with losses *a*) series- and *b*) parallel-model (From Paper II).

Until here, the presence of the eddy currents has been related to the problematic of the losses and to how these affect the resistive part of the winding impedance. In Figure 11, the reaction of the eddy currents towards the magnetic flux is represented by means of two magnetic circuits, a solid one *a*) and a laminated one *b*).

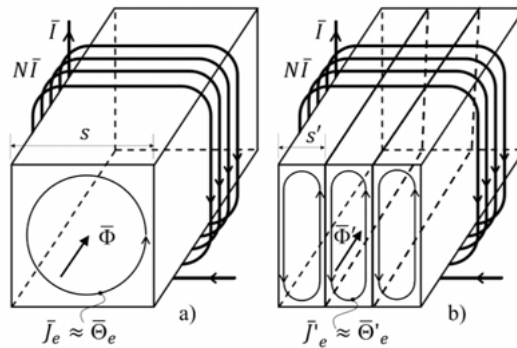


FIGURE 11 – Eddy currents in a solid *a*) and laminated *b*) magnetic circuit.

The same sinusoidal MMF, $N\bar{I}$, establishes the fluxes, $\bar{\Phi}$ and $\bar{\Phi}'$, in the first and in the second magnetic circuit respectively, which are assumed as having linear and isotropic properties for simplicity. These fluxes are produced by the simultaneous actions of the impressed MMF, $N\bar{I}$, on the one side and the induced $\bar{\Theta}_e$ and $\bar{\Theta}'_e$ respectively, on the other side. Due to the Lenz's law, the eddy currents counteract the action of the external MMF. However, the effectiveness of their opposition depends on the resistance and inductance of the path followed by the eddy current density in the magnetic circuit. With reference to Figure 12, considering the unitary length of a partially penetrated² ferromagnetic lamina with dimension $b \gg w$, the ratio between the reactance and the resistance sensed by the eddy currents per unit length [21] is

$$\frac{\omega l_e}{r_e} \cong \omega \mu b w \frac{\delta}{2 \rho b} = \frac{w}{\delta}, \quad (8)$$

where

$$\delta = \sqrt{\frac{2\rho}{\omega\mu}} \quad (9)$$

is the penetration depth of the eddy current density in the lamina for a given angular frequency ω .

Equation (8) shows that the shorter the penetration depth the higher the relative magnitude of the reactance to the resistance of the eddy current circulation path. Therefore, it is expected that a partially penetrated ferromagnetic circuit can oppose the establishment of the variable magnetic flux more effectively than a fully penetrated one.

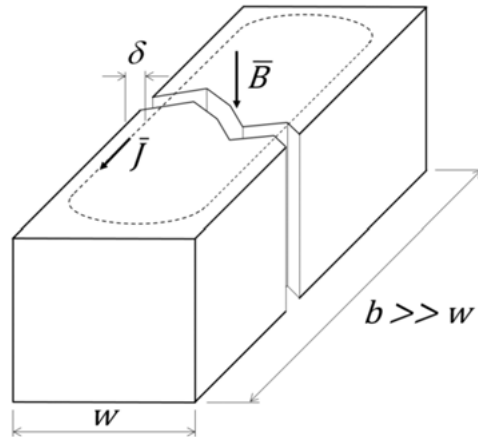


FIGURE 12 –resistance and reactance experienced by the eddy currents (From Paper IV).

² A conductor is partially penetrated when δ does not exceed the smallest of its dimensions.

With reference to the magnetic circuit in Fig. 11a, the composition of the MMFs, $N\bar{I}$ and $\bar{\Theta}_e$, which results in the flux, $\bar{\Phi}$, is depicted in Figure 13.

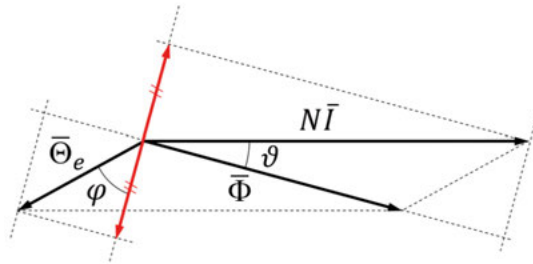


FIGURE 13 – The composition of the impressed and induced MMFs.

A first fact to be observed in Fig. 13 is that the total flux lags the MMF due to the presence of the eddy currents. This result represents the macroscopic evidence of the local property already stated by (1).

A second relevant observation is that the sum of the projections of the MMFs on the axis perpendicular to the direction of the phasor $\bar{\Phi}$ must be equal to zero for the principle of energy conservation. In fact, $j\omega\bar{\Phi}$ represents the induced EMF for each single turn of the winding. In this respect, the MMF of the eddy currents can be regarded as produced by the short-circuit current of a transformer with a single secondary turn, so that

$$NI \sin \vartheta = \Theta_e \cos \varphi. \quad (10)$$

Since the angle φ expresses how much $\bar{\Theta}_e$ lags on the EMF induced in the magnetic circuit, with reference to Fig. 11a and (8), it is found that

$$\tan \varphi = \frac{\omega l_e}{r_e} = \frac{s}{\delta}. \quad (11)$$

Since the DC inductance of the winding in Fig. 11a is defined by the real part of (2) as

$$L_{DC} = \frac{N^2}{\mathcal{R}} = \left(\frac{NI}{I}\right) \frac{N}{l}, \quad (12)$$

the AC inductance L , by means of Fig. 13, must be

$$L = \left(\frac{NI \cos \vartheta - \Theta_e \sin \varphi}{\mathcal{R}}\right) \frac{N}{I \cos \vartheta} = L_{DC} \left(1 - \frac{\Theta_e \sin \varphi}{NI \cos \vartheta}\right). \quad (13)$$

Considering (10) and (11), after simple trigonometric passages, equation (13) becomes

$$L = L_{DC} \left\{ 1 - \frac{\Theta_e}{NI} \frac{1}{\sqrt{1 + \left(\frac{\delta}{s}\right)^2 \left[1 - \left(\frac{\Theta_e}{NI}\right)^2\right]}} \right\}. \quad (14)$$

When the ferromagnetic circuit is fully penetrated ($\delta \gg s$) the AC inductance (14) approximates the DC one. On the contrary, when the ferromagnetic circuit is partially penetrated ($\delta \ll s$), the AC inductance tends to its minimal value

$$L_{min} = L_{DC} \left(1 - \frac{\Theta_e}{NI}\right). \quad (15)$$

It must be observed in (8) that, when $\delta \ll s$ the nature of the path for the eddy currents is essentially inductive so that, according to the transformer like analogy, the MMFs in play are the short circuit ones essentially, with $\Theta_e \cong NI$. This fact lets conclude that L_{min} can be much smaller than L_{DC} .

With reference to Fig. 11b, the consequence of laminating the magnetic circuit is that the condition for the partial penetration $\delta < s'$ requires a higher frequency than in Fig. 11a in order to be fulfilled. This means that for the same frequency an inductor with laminated circuit presents a higher inductance than one with a solid magnetic circuit [22].

Figure 14 shows, e.g., how the lamination thickness $s' = s/10$ improves the frequency response of the inductor by increasing its cutoff frequency. The magnetic circuits related to Fig. 14 have $\Theta_e(\omega \rightarrow \infty) = 0.9 NI$, which explains why $L_{min} = 0.1 L_{DC}$.

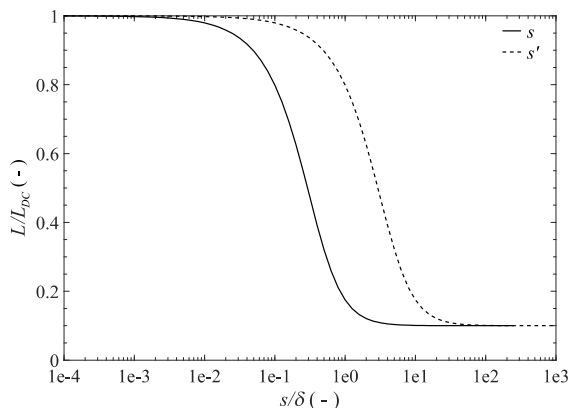


FIGURE 14 – The effect of magnetic circuit lamination on the inductance.

Therefore, a further effect produced by the eddy currents in the magnetic circuit of an inductor is that of decreasing the winding AC-inductance. Free circulating eddy currents in the magnetic circuit impair the capacity of the winding MMF to build a magnetic flux.

In other words, if the eddy currents can circulate in the magnetic circuit, in order to keep the magnetic flux amplitude constant when the frequency increases, a larger and larger exciting MMF is needed.

2.2. The distributed parameters model of the winding and the travelling waves

The homogenous properties of the excitation winding in salient pole synchronous machines make it possible to represent the electromagnetic phenomena taking place in the copper wire, in the insulating material and in the ferromagnetic circuit respectively, as uniformly distributed along the wire length.

This kind of representation, inspired by the Telegrapher's equations of O. Heaviside [23], is known as Single Transmission Line Model (STLM) of the winding. It is a particular application of the more general theory of the Multiconductor Transmission Line Model (MTLM) [24]. An infinitesimal portion dx of the excitation winding, taken at the distance x from one of its terminals, is represented in Figure 15.

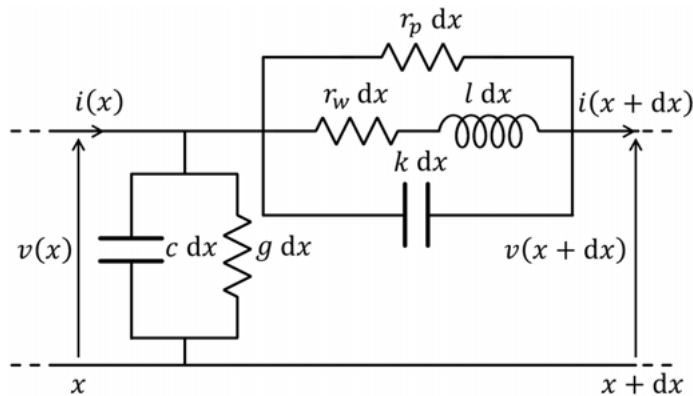


FIGURE 15 – Single Transmission Line Model of the winding (From Paper IV).

The specific capacitance of the winding towards the machine frame is taken into account by the specific turn-to-ground capacitance, c ($\text{F}\cdot\text{m}^{-1}$), since the structural parts of the synchronous machine are normally connected to potential of the ground. The parameter, k ($\text{F}^{-1}\cdot\text{m}^{-1}$), describes the specific electrostatic induction between two adjacent turns of the winding and it is called turn-to-turn specific elastance. All magnetic causes, responsible for inducing an electromotive force (EMF) into the winding, are represented by the specific winding inductance, l ($\text{H}\cdot\text{m}^{-1}$). Finally, all dissipative phenomena occurring in the winding are addressed in the circuit through three distinct parameters: the specific winding AC-resistance, r_w ($\Omega\cdot\text{m}^{-1}$), which considers the wire Joule losses in presence of skin and proximity effect; the parallel resistance, r_p ($\Omega\cdot\text{m}^{-1}$), which relates to the magnetic losses; the specific conductance, g ($\text{S}\cdot\text{m}^{-1}$), which takes into account the dielectric losses.

The distributed parameters used in the model are specific quantities expressed per unit length of the winding wire.

In order to present some important properties of the winding, the dissipative parameters r_w , r_p and g can be neglected in a first analysis. The influence of the dissipative parameters on the overvoltage attenuation can be better represented in the frequency domain at a later moment. Therefore, the reference STLM model of the field winding becomes the one depicted in Figure 16.

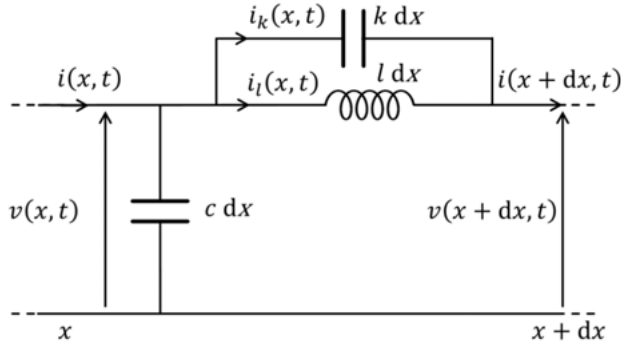


FIGURE 16 – Lossless Single Transmission Line Model of the winding.

In Appendix 1, it is shown how the turn-to-ground voltage $v(x, t)$ and the current in the turn $i_l(x, t)$ at the generic coordinate x along the winding must satisfy the following partial differential equations

$$\frac{\partial^2 v}{\partial x^2} - lc \frac{\partial^2 v}{\partial t^2} + \frac{l}{k} \frac{\partial^4 v}{\partial x^2 \partial t^2} = 0 \quad (16)$$

$$\frac{\partial^2 i_l}{\partial x^2} - lc \frac{\partial^2 i_l}{\partial t^2} + \frac{l}{k} \frac{\partial^4 i_l}{\partial x^2 \partial t^2} = 0 \quad (17)$$

respectively.

Equations (16) and (17) resemble those describing the Transverse Electromagnetic (TEM) propagation of voltage- and current-wave in a lossless transmission line [25]. The only difference between the first ones and the second ones consists in the fourth order mixed partial derivatives. These are introduced in (16) and (17) by the presence of the inter-turn specific elastance, k , and are responsible for the dispersive behavior of the field winding towards voltage and current waves. In fact, the dispersive behavior in a transmission lines is solely related to the presence of the dissipative parameters r and g , as the Heaviside condition stresses [26]. Otherwise, the propagation speed u_{TEM} is constant

$$u_{TEM} = \frac{1}{\sqrt{lc}} \quad (18)$$

and the wave number grows linearly with the frequency

$$\beta = \omega \sqrt{lc}, \quad (19)$$

avoiding, in this way, the phase distortion of the propagating wave.

In contrast with that, the field winding is always dispersive, even in the absence of dissipative phenomena.

The formula of the wave propagation speed, u , for the lossless model in Fig. 16 (Appendix 2), shows that the voltage and current waves propagate at lower speed than the TEM wave, u_{TEM} , and precisely

$$u = \frac{\omega}{\beta} = \frac{1}{\sqrt{lc + \beta^2 \frac{l}{k}}} = \frac{u_{TEM}}{\sqrt{1 + \beta^2 \frac{1}{ck}}}. \quad (20)$$

The wavenumber, β , increases when the frequency increases due to the shorter and shorter wavelength. Hence, it can be concluded through (20) that low-frequency harmonic waves travel in the winding at faster speed than the high-frequency ones. This proves the dispersive nature of the field winding, which discriminates between harmonic waves showing different frequency. The very low frequency harmonic waves can propagate at a speed which is

$$u_{TEM} = \frac{c_0}{\sqrt{\epsilon_r}}, \quad (21)$$

where c_0 is the speed of light in vacuum and ϵ_r the relative permittivity of the winding insulating material. The high frequency harmonics waves can show a propagation speed much lower than u_{TEM} . In particular, the frequency for which the wavenumber becomes infinite is called critical frequency of the field winding

$$\omega_c = \sqrt{\frac{k}{l}}. \quad (22)$$

It corresponds to the frequency for which the wave propagation speed becomes zero, meaning that the propagation phenomena described by (16) and (17) can only be possible for frequencies below the critical one. This fact introduces a difference in the behavior of the field winding with reference to two separated ranges of frequency, the subcritical ($0 < \omega \leq \omega_c$) and the supercritical ($\omega > \omega_c$) ones respectively. The difference between these two behaviors, which plays a fundamental role in the occurrence of voltage surges in the winding, can be better shown and explained in the frequency domain.

2.3. The distributed parameters model in the frequency domain

With reference to the theory of transmission lines, the voltage \bar{V}_x and the current \bar{I}_x at the coordinate x in a uniform single transmission line are given by

$$\begin{cases} \bar{V}_0 = \cosh(\bar{K}x)\bar{V}_x + \bar{Z}_0 \sinh(\bar{K}x)\bar{I}_x \\ \bar{I}_0 = \frac{1}{\bar{Z}_0} \sinh(\bar{K}x)\bar{V}_x + \cosh(\bar{K}x)\bar{I}_x \end{cases} \quad (23)$$

where \bar{K} and \bar{Z}_0 represent the propagation constant and the characteristic impedance of the line respectively. With reference to the distributed parameters model in Fig. 15, the propagation constant is equal to

$$\bar{K} = \sqrt{\bar{z} \cdot \bar{y}} = \sqrt{\left(\frac{1}{r_p} + \frac{1}{r_w + j\omega l} + \frac{j\omega}{k}\right)^{-1} \cdot (g + j\omega c)} \quad (24)$$

and the characteristic impedance to

$$\bar{Z}_0 = \sqrt{\frac{\bar{z}}{\bar{y}}} = \frac{1}{\sqrt{\left(\frac{1}{r_p} + \frac{1}{r_w + j\omega l} + \frac{j\omega}{k}\right) \cdot (g + j\omega c)}} \quad (25)$$

In order to find the voltage distribution along the winding ($0 \leq x \leq a$) at different frequencies, two different and extreme load conditions at the end of the line can be envisaged:

- a) the short circuit one, which consists in grounding the ending terminal of the winding;
- b) the open circuit one, which considers the ending terminal open with its potential floating.

For the case a), the following voltage distribution can be easily found from (23)

$$\bar{F}_{x,sc} = \frac{\bar{V}_x}{\bar{V}_0} = \frac{\sinh[\bar{K}(a-x)]}{\sinh(\bar{K}a)} \quad (26)$$

whereas, for the case b),

$$\bar{F}_{x,oc} = \frac{\bar{V}_x}{\bar{V}_0} = \frac{\cosh[\bar{K}(a-x)]}{\cosh(\bar{K}a)} \quad (27)$$

The condition a) is more interesting for power electronics applications, since the winding terminals are usually connected to well definite potentials, either the link voltage or the ground voltage.

Imagining the field winding excited by an AC voltage with amplitude V_{in} at its beginning, as shown in Figure 17, the propagation of the voltage waves forth and back in the winding must produce a perturbation $\delta V(x)$ of the otherwise linear voltage to ground distribution.

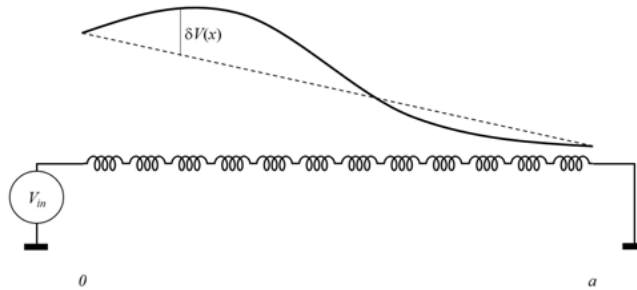


FIGURE 17 – Voltage deviation from the linear distribution (From Paper I).

The voltage perturbation must be forcibly zero at the beginning and at the end of the winding, since the potentials of those points are fixed.

This implies that the standing wave, produced by the superposition of the waves travelling in the winding, must account for an integer number of half waves or, what is the same,

$$\beta_m a = m\pi \quad (m = 1, 2, 3 \dots). \quad (28)$$

The wave number β_m , which corresponds to the m -th resonance mode of the winding when one of its terminals is grounded, can be determined from (24) considering the lossless case

$$\bar{K}_m = j\beta_m = j\omega_m \sqrt{\frac{kcl}{k - \omega_m^2 l}} \quad (29)$$

Substituting the value of β_m obtained from (29) in (28) and solving for ω_m , the following expression is obtained

$$\omega_m = \frac{1}{\sqrt{lc\left(\frac{a}{m\pi}\right)^2 + \frac{l}{k}}} \quad (30)$$

Equation (30) represents the numerical sequence of all possible natural frequencies of the field winding, when it is grounded at one terminal. The sequence (30) converges to the critical frequency (22) for $m \rightarrow \infty$. In Appendix 3, it is shown that the resonance frequencies of the winding are smaller than the corresponding natural frequencies (30), due to the presence of the dissipative parameters. Considering ζ_m as the damping coefficient of the winding at the m -th winding resonance frequency

$$\zeta_m = \frac{\omega_m}{2} \left[\frac{l}{r_p} + gl \left(\frac{a}{m\pi} \right)^2 \right], \quad (31)$$

the resonance frequency results

$$\omega_{r,m} = \omega_m \sqrt{1 - \zeta_m^2}. \quad (32)$$

Equation (31) shows that the damping effect of the winding losses on the voltage waves increases with the frequency. The eddy current losses are mainly responsible for that, since the losses in the insulation decrease with the increasing order of the considered resonance. Figure 18 represents the voltage to ground distribution (26), $\bar{F}_{x,sc}(x/a, \omega/\omega_c)$, as a function of the normalized position and frequency. The distribution takes into account the losses in the winding through the dissipative parameters. In that way, where the distribution presents the relative maxima, the corresponding frequencies are resonance frequencies (32). In Fig. 18, it can be recognized that the sequence of the resonance frequencies converges to the critical frequency while the amplitude of the corresponding relative voltages decreases.

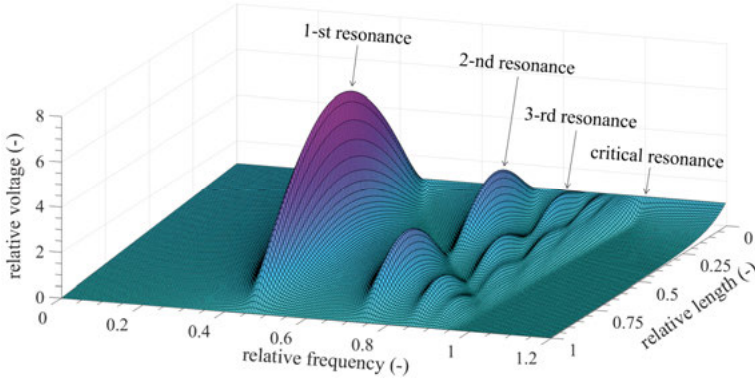


FIGURE 18 – Several resonance modes of the field winding.

The critical frequency represents the ultimate resonance frequency. In fact, the winding does not resonate anymore beyond the critical frequency. The reason for that is the nature assumed by the specific series impedance \bar{z} . The critical frequency also represents the parallel resonance frequency of the circuit in Fig. 15. For frequencies higher than the critical one the series impedance \bar{z} definitively works as a capacitive load, making it impossible for the specific capacitance c to give rise to a series resonance. Since the periodic energy exchange between distributed inductance and capacitance is not possible anymore, the propagation of the voltage along the winding happens by means of the electrostatic induction, so that the current in the winding represents the displacement current through the turn-to-turn elastance essentially. That gives to the voltage distribution the characteristic pseudo-exponential decay versus x , which can be observed in Fig. 18 for frequency higher than the critical one.

Therefore, when the circuit in Fig. 15 reduces to the specific capacitances at high frequency, the propagation constant becomes a real number which depends on the ratio between the winding capacitance to ground and the turn-to-turn capacitance essentially

$$\bar{K}_\infty = \sqrt{kc} = \frac{1}{a} \sqrt{\frac{c_p}{c_s}} \quad (33)$$

In Appendix 4, it is shown that the specific voltage gradient at the beginning of the winding depends on the propagation constant according to

$$\frac{1}{V} \frac{dV}{dx} \Big|_{x=0} \approx -\|\bar{K}\|. \quad (34)$$

Therefore, the specific gradient at the critical frequency is

$$\frac{1}{V} \frac{dV}{dx} \Big|_{x=0} \approx -\|\sqrt{r_p j \omega_c c}\| = -\sqrt{kc} \sqrt{\frac{r_p}{\omega_c l}} = -K_\infty \sqrt{Q_c}, \quad (35)$$

whereas, at high frequency, it results

$$\left. \frac{1}{v} \frac{dV_\infty}{dx} \right|_{x=0} \approx -\|\bar{K}_\infty\| = -\sqrt{kc}. \quad (36)$$

Comparing (35) and (36), it can be recognized that the voltage gradient at the critical frequency can be harsher than the one at high frequency, if the quality factor of the winding at the critical frequency is larger than one

$$Q_c > 1. \quad (37)$$

However, considering the low value of the winding quality factor for solid pole WFSM windings at the first resonance frequency ($Q \cong 1 \div 3$) and taking into account the increasing eddy current losses when the frequency increases, it can be realized that (37) can hardly be fulfilled. Hence, the high frequency gradient remains the most important gradient in the field winding for all the cases of practical interest.

2.4. The importance of the modal dispersion

Many works studying transients in the windings of electrical machines make use of lumped circuit models. The reason for that is the simplicity in solving discrete components circuits in the time domain, especially if they are linear and present constant parameters. Since the lumped model is a discrete approximation of the real continuous object of study, some attention must be paid to the choice of the minimal number of elements, in which the real object must be broken into. In the end, this choice affects the accuracy of the simulations obtained through the lumped circuit model itself. One of the most important fact to pay attention to is that the assumption of considering the voltage or current constant in each single lumped element reflects, as good as possible, the real behavior in the winding. Therefore, said a the length of the winding and n the number of lumped cells in cascade approximating the distributed parameter model, the condition

$$\lambda_m \gg \frac{a}{n} \quad (38)$$

ensures that the voltage or current propagation time within each lumped-cell is negligible in comparison to the wave period of the studied m -th harmonic. Therefore, considering or neglecting the presence of the modal dispersion in the winding can make a remarkable difference in the outcome of (38). This can be shown by means of two examples about the same winding. The first case takes into account the modal dispersion. Hence, if the harmonics of interest are those below the m -th natural frequency of the winding, considering (20) and (28), condition (38) becomes

$$\frac{u_m}{f_m} = \frac{2a}{m} \gg \frac{a}{n_m} \rightarrow n_m \gg \frac{m}{2}. \quad (39)$$

The twelfth natural frequency of the field winding for the 60 kVA synchronous generator studied in Paper 3 corresponds to $f_{12}=94.75$ kHz. The correspondent propagation speed results $u_{12}=8.1 \cdot 10^6$ m/s, whereas the winding length is $a=1027$ m. If the operator “ \gg ” means, e.g., 10 times at least, according to (39), in order to properly consider the frequencies till the 12th resonance frequency, a minimum of 60 cells is needed in the lumped circuit model. The second example does not pay attention for the modal dispersion. According to a recurring assumption made in many works on this matter [27-31], the propagation speed in the windings is assumed constant as the voltage or current transmission through the winding were a TEM one. Assuming for the winding insulation $\epsilon_r=2.4$ and considering (21), condition (38) becomes

$$\frac{c_0}{\sqrt{\epsilon_r} f_{12}} \gg \frac{a}{n} \rightarrow n \gg \frac{a\sqrt{\epsilon_r} f_{12}}{c_0} = 0.5. \quad (40)$$

Having neglected the modal dispersion, it seems that a cascade of $0.5 \times 10 = 5$ lumped cells is enough for correctly describing the behavior of the winding up to the twelfth natural frequency of the winding. But the number of the needed cells evidently results underestimated. In fact, the propagation time in one-fifth of the winding length is in the end larger than the period of the twelfth natural frequency

$$\frac{a}{5u_{12}} = 25.3 \mu\text{s} > \frac{1}{f_{12}} = 10.3 \mu\text{s}, \quad (41)$$

which openly contradicts condition (38).

If the order of the last significant harmonic, which the lumped circuit aims to reproduce, is close to the winding critical frequency, the number of the needed cells could increase significantly. This is due to the very low propagation speed (20) presented by the highest natural frequencies. This fact could jeopardize the advantage of using a simplified lumped-circuit model over a distributed parameters one, when the number of cell to be used is anyway considerable. Moreover, the dependence of both inductance (6) and apparent resistance (7) of the field winding on the frequency makes the constants of the lumped circuit dependent on the frequency too. The resolution of Ordinary Differential Equations (ODE) with frequency dependent parameters requires special algorithms involving convolution integrals [32]. This fact makes the complexity of the computational problem in the time domain even heavier.

2.5. A frequency dependent winding model

For the reasons presented in the previous paragraph, this work has focused the attention on the construction of a distributed parameters model for the field winding, with frequency dependent constants. The goal is that to obtain the Transfer Function (TF), $\bar{F}_{x,sc}(x, j\omega)$, given in (26) in order to express the turn-to-ground voltage, $\bar{V}_x(x, j\omega)$, at a generic distance x from the applied input voltage, $\bar{V}_0(j\omega)$. The input voltage is the Fourier Transform (FT) of a generic applied voltage, $v_0(t)$, according to

$$\bar{V}_0(j\omega) = \int_{-\infty}^{+\infty} v_0(t)e^{-j\omega t} dt. \quad (42)$$

The response of the winding in the time domain, $v_x(t)$, can be achieved by anti-transforming the correspondent frequency response at the progressive x by

$$v_x(t) = \frac{1}{2\pi} \int_{-\infty}^{+\infty} \bar{F}_{x,sc}(x, j\omega) \bar{V}_0(j\omega) e^{j\omega t} d\omega. \quad (43)$$

The construction of the integrand function in (43) does not pose special difficulties, even though the TF shows frequency dependent parameters. In the frequency domain, it just takes a multiplication of functions whereas, in the time domain, it would require their convolution.

The voltage signals considered by this research are the rapid front edges produced by the fast switching of power electronics switches. Examples of this kind of voltage functions are those presented in Figure 19.

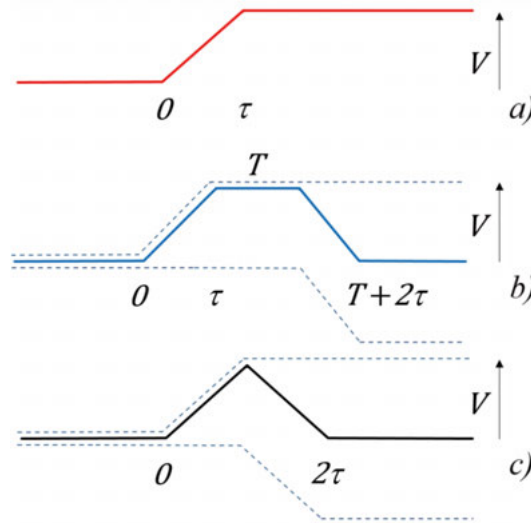


FIGURE 19 – Voltage signals related to the same rise-time τ (from Paper IV): a) step function, b) pulse with duration T , c) triangular pulse.

These voltage profiles take all the same rise time, τ , in order to reach the same maximal voltage, V . The step function *a*) holds the reached voltage V indefinitely, the pulse *b*) for a finite time T , whereas the triangular pulse *c*) just for an instant. It is to be expected, that these different features in the time domain plant some differences in the spectral densities of the considered signals. At the same time, as shown in Fig. 19 through the shaded profiles, all three signals have something in common, since they can be obtained by superposition of the same step function differently delayed and mirrored. In Figure 20, the voltage spectral densities of the three signals are represented for $T=10\ \mu\text{s}$ and $\tau=10\ \text{ns}$.

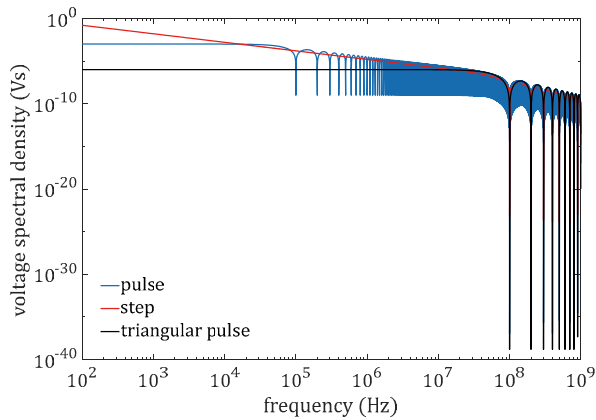


FIGURE 20 – Voltage densities of the three signals in Fig.19 having the same rise-time $\tau=10\ \text{ns}$ and the same maximal voltage $V=100\ \text{V}$ (from paper IV).

It can be noticed that the strongest difference between the step function and the pulse takes place for frequency lower than $1/T$ essentially. Otherwise, the three voltage profiles share almost the same spectrum for frequency higher than $1/\tau$. This fact clearly points to a correspondence between the common rising front of the signals and the common harmonic content of the spectral densities beyond the frequency $1/\tau$. Therefore, if the effect of the rapid voltage edges must be caught by the proposed model, the model must be able to reproduce the behavior of the winding at high frequency. For all the reasons presented so far, Paper III has been dedicated to the determination of a distributed parameters model of the field winding which:

- a) takes into account the modal dispersion,
- b) has frequency dependent parameters and
- c) is able to reproduce the winding behavior at high frequency.

3. Methods

3.1. The analysis of the winding transfer function

The analysis of the fast switching voltage front in the previous paragraph has shown that the rapid variation of the voltage applied to the winding is related to the highest spectral lines of the signal spectrum. The time response produced in the winding by such a signal must contain the same lines but with some changes in their amplitudes and phases operated by their passage through the winding itself. For this reasons, the TF of the model representing the field winding must be able to reproduce the frequency response of the field winding, in a broad range of frequency. This would make sure that all the needed information about the winding voltage response is available and complete in the frequency domain. Therefore, the knowledge of the winding behavior in the frequency domain is a key passage in the construction of the model. In the literature, it is possible to find many references about the experimental setups for obtaining the TF of a winding. In particular, the technique called Frequency Response Analysis (FRA) [33-36] makes use of the TF in order to detect fault conditions or unwanted structural/functional changes in the windings. This consists in supplying the winding, or a portion of it, by a known sinusoidal voltage with adjustable frequency (input) and measuring the resulting voltage or current in another point of the winding (output). The complex function which correlates the specific output quantity to the input quantity depends on the frequency and characterizes the TF of the winding at the specific chosen measurement point. In Paper I, the setup reproduced in Figure 21a has been used. It consists of a square wave inverter having the field winding connected to the poles of the inverter legs. Each pole voltage can be represented through its AC and DC components (Fig. 21b), which reveal the presence of a DC-bias (common mode voltage) in the setting. Figure 21c shows the sole AC components (differential mode voltage) supplying the winding. The application of a square wave voltage to the winding does not represents a limitation for the harmonic analysis, since the very low cutoff frequency of the winding attenuates the higher harmonics much more than the fundamental one.

Figure 22 shows the result of the strong input signal filtering caused by the winding. However, a drawback of this setting is that the middle point O of the winding assumes a specific voltage and cannot be forced to ground in order to have a sure potential reference. Therefore, the use of the inverter shown in Fig. 21 does not allow to connect a single point of the winding to a fixed potential.

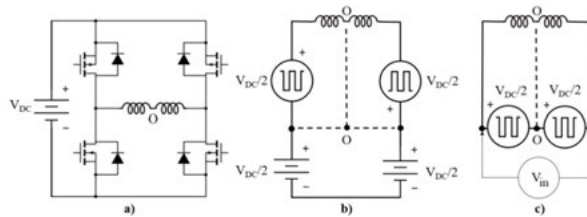


FIGURE 21 – The square wave inverter for supplying the winding: a) H-bridge, b) DC and AC voltages, c) differential mode voltages (from Paper I).

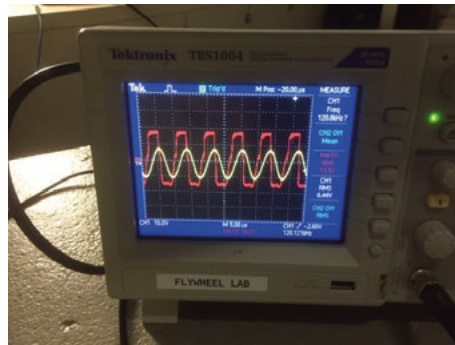


FIGURE 22 – A sinusoidal output voltage got from a square wave input.

For this reason the setup in Figure 23 has been adopted in the end, where the winding is earthed at one terminal, while it is supplied by a sinusoidal voltage source with variable frequency at the other one.

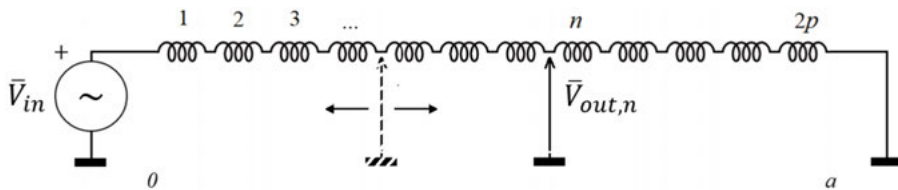


FIGURE 23 – 2p points of measure for the winding voltage to ground (redapted from Paper I)

In this setup, one point of the winding is permanently and effectively connected to the ground potential, whereas the node O, in the middle of the winding is free to assume different voltages. This allows to detect a lower resonance frequency in the winding, where the half-wave of the

voltage acts over $2p$ poles instead of p poles only (Fig. 21c). Moreover, all the connection points between the adjacent pole-windings (referred as winding taps in the thesis) are accessible for measuring the winding voltage to ground without any need to remove the insulation in other point of the winding. That makes it possible to detect $2p$ transfer functions along the winding, just by changing the position where the output voltage needs to be measured.

3.2. The experimental determination of the parameters

The adopted distributed parameters model for the field winding in the frequency domain is represented in Figure 24, where only four of the six parameters shown in Fig. 15 need to be determined.

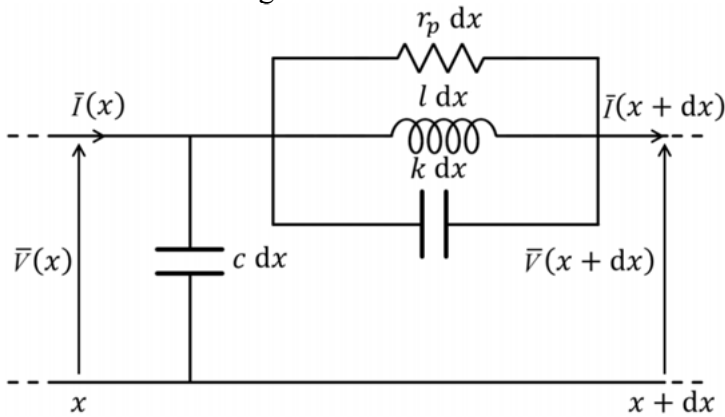


FIGURE 24 – model for the field winding in the frequency domain (readapted from paper IV).

The specific conductance g and the wire specific AC-resistance r_w have been neglected in the model. The specific conductance g is related to the losses in the insulation and, in Appendix A.3, it is shown that the relative importance of the dielectric losses to the eddy current losses decreases with the increasing frequency. The skin- and proximity effect cause the increase of the winding AC-resistance with the frequency since the conduction current gets confined in a smaller and smaller portion of the wire cross-section, the dimension of which is determined by the penetration depth. Therefore, while the winding resistance grows according to the square root of the frequency, the winding reactance grows almost linearly with the frequency, since the inductance reduces to the winding stray inductance in air in the worst case scenario. This fact suggests that, in the end, the conduction current in the wire is limited by the winding inductance essentially.

3.2.1. The parasitic capacitances of the winding

Equation (36) shows that, for frequency larger than the critical one, the initial gradient of the voltage distribution along the winding depends on the ratio between the capacitances C_p and C_s . With reference to Figure 25, measuring the voltage to ground between the first and the second pole-winding (setup in Fig. 23), three points of the relative voltage distribution get determined: the input voltage equal to 1, the first pole voltage to ground v_1 and the end voltage equal to zero.

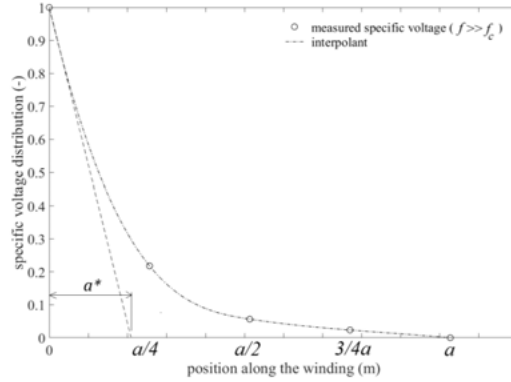


FIGURE 25 – Relative voltage distribution at high frequency.

This data is enough for plotting the entire voltage profile, since the propagation constant, K_∞ , can be found by numerically solving the equation

$$v_1 = \frac{\sinh\left[K_\infty \frac{2p-1}{2p} a\right]}{\sinh(K_\infty a)}. \quad (44)$$

Once K_∞ is known, the ratio between C_p and C_s can be easily determined from (33) by

$$\frac{c_p}{c_s} = (K_\infty a)^2. \quad (45)$$

Alternatively, by measuring the voltages at two internal points in the winding, and by knowing the initial and final values of the voltage distribution, a least mean squares fitting curve

$$y = c_1 e^{b_1 x} + c_2 e^{-b_2 x} \quad (46)$$

can be found. At this point, the propagation constant, K_∞ , can be determined in two different ways. The first way makes use of the derivative at $x=0$ of (46)

$$K_\infty = (c_1 b_1 - c_2 b_2). \quad (47)$$

The second way considers the intercept, a^* , on the x -axis taken by the tangential straight to the fitting curves (46) at $x=0$

$$K_{\infty} = \frac{1}{a^*}. \quad (48)$$

However, the knowledge of the propagation constant at high frequency, K_{∞} , can only provide the ratio between the winding parasitic capacitances (45). In order to determine C_p , the largest one of the two capacitances, the principle of the capacitive voltage divider can be used, as it is shown in Figure 26.

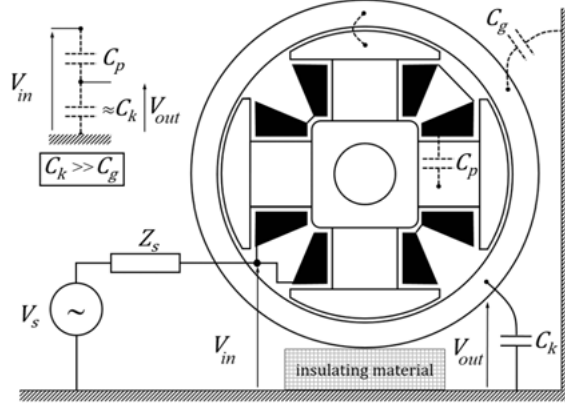


FIGURE 26 – Setup for measuring C_p and C_g (readapted from Paper III)

The capacitance towards ground for the machine frame or the rotor can roughly be estimated through the formula

$$C_g \cong 2\pi\epsilon_0 d, \quad (49)$$

where ϵ_0 is the permittivity of the vacuum and d the machine or rotor diameter respectively. Equation (49) indicates that the ground capacitance, C_g , has the order of magnitude of tenths or hundreds of picofarad. If a ballast capacitor of known capacitance, C_k , is used for grounding the machine frame, the same goes in parallel to the capacitance C_g . As soon as a low frequency sinusoidal potential with amplitude V_{in} is forced at the two terminals of the field winding, a voltage divider is build up between C_p on the one side and the parallel of C_g and C_k on the other side. If the ballast capacitance is two orders of magnitude larger than C_g , the potential, V_{out} , assumed by the machine frame, depends on V_{in} , C_p and C_k . essentially. Therefore, the capacitance, C_p , can be indirectly measured by using the measured potential V_{out} in the formula

$$C_p \cong C_k \frac{1}{\frac{V_{in}}{V_{out}} - 1}. \quad (50)$$

Once C_p is known, C_s is easily obtained from (45).

3.2.2. The parallel resistance of the winding

With reference to Figure 27, the elements of the lumped-circuit enclosed by the shaded box represent the field winding parameters. The elements outside the box are related to the external components, such as the sinusoidal voltage generator, \bar{V}_s , with its internal impedance, Z_s , the external ballast capacitor, C_k , the ground capacitance of the machine frame, C_g , and the resistive load, R_k .

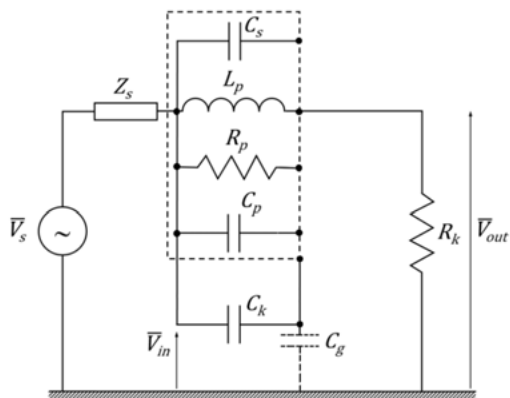


FIGURE 27 – Setup for determining R_p (from Paper III)

Since the capacitance, C_g , accounts for hundreds of picofarad, it is in general much smaller than the capacitance, C_p , or the ballast capacitance, C_k , which range in the order of nanofarad. This is the reason why the ground capacitance, C_g , can be considered an open circuit, at least for frequencies below the first natural one. Therefore, the capacitances C_s , C_p and C_k , form a single large capacitance in parallel with the winding inductance, L_p , and the winding parallel resistance, R_p . The described topology represents a parallel resonant circuit with resonance frequency

$$f_0(C_k) \cong \frac{1}{2\pi} \frac{1}{\sqrt{L_p(C_s+C_p+C_k)}}. \quad (51)$$

For frequencies lower than f_0 , the circuit portion inside the shaded box in Fig. 27 shows a predominant inductive nature; whereas, for frequencies higher than f_0 , it turns into a resistive-capacitive load. At the resonance frequency, f_0 , the capacitive and inductive reactance of the same circuit portion cancel out, so that the circuit inside the shaded box reduces to the sole resistance, R_p . This is the sole condition, where the voltage divider, having \bar{V}_{in} as the input and \bar{V}_{out} as the output, does not cause any phase displacement between the two sinusoidal voltages. This fact can be easily detected by sensing \bar{V}_{in} on the channel X and

\bar{V}_{out} on the channel Y of an oscilloscope, when the XY-mode of visualization is activated on the screen. When the circuit in Fig. 27 is out of resonance, a more or less pronounced elliptical trace will appear on the oscilloscope screen as shown in Figure 28. As soon as the same circuit is in resonance, the elliptical trace turns into a straight segment with a positive slope instead.

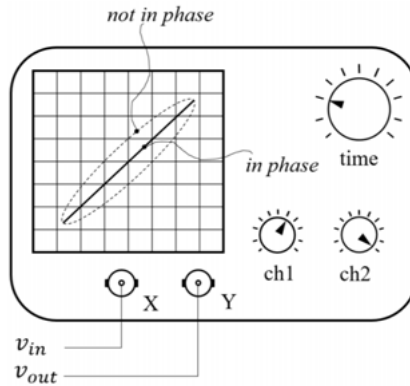


FIGURE 28 – The Lissajous figures help to detect the resonance condition (from Paper III).

By selecting a certain value of the ballast capacitance, C_k , a unique parallel resonance frequency, $f_0(C_k)$, for the circuit in Fig. 27, is determined. By adjusting the frequency of the sinusoidal voltage generator, the circuit can be set into resonance, where the observation of the trace shape on the oscilloscope helps to recognize when the resonance is met. Under that condition, the knowledge of the resistance value, R_k , and the measurements of the input and output voltages, \bar{V}_{in} and \bar{V}_{out} , allow the indirect determination of the resistance, $R_p(f_0)$, by

$$R_p(f_0) = R_k \left(\frac{V_{in}}{V_{out}} - 1 \right). \quad (52)$$

Since the resonance frequency can be changed by changing the value of the external capacitance, C_k , given a set of different ballast capacitances $[C_k]$, a set of different resonance frequencies $[f_0]$ can be targeted. This makes it possible to measure several values of R_p by (52), each one corresponding to a specific resonance frequency. An experimental dependence of the parallel resistance, R_p , on the frequency, f_0 , can be graphically expressed through a set of points, the coordinates of which are $[f_0, R_p]$.

In order to evaluate how strongly the resistance, R_p , depends on the frequency, the sequence of points $[f_0, R_p]$ can be fitted by the function

$$R_p(f) = Hf^\sigma. \quad (53)$$

The coefficients H and σ are the outcomes of the fitting operation.

3.2.3. The inductance of the winding

In Paper II, it has been shown that the winding inductance decreases when the frequency increases, due to the degaussing effect of the eddy currents. Therefore, a frequency dependent parameter, l , for the specific inductance must be taken into account in the distributed parameter model in Fig. 24. This fact introduces some difficulties not only in solving the equations (16) and (17) in the time domain, but also in determining the natural frequencies in the frequency domain. From (30), it can be recognized that the natural frequency depends on the winding inductance, which in turn depends on the natural frequency

$$f_m = \frac{1}{2\pi} \frac{1}{\sqrt{l(f_m) \left[c \left(\frac{a}{m\pi} \right)^2 + \frac{1}{k} \right]}}. \quad (54)$$

Therefore, an iterative method would be needed in order to determine f_m . Nevertheless, if a simple inductance law is assumed for the field winding, such as

$$l = \frac{K}{a} f^\gamma, \quad (55)$$

the parasitic capacitances of the winding can be related to the first and the m -th generic winding natural frequency by (Appendix A.5)

$$C_p = \frac{1}{K(m^2-1)} \left[\frac{1}{(f_1)^{2+\gamma}} - \frac{1}{(f_m)^{2+\gamma}} \right] \quad (56)$$

and

$$C_s = \frac{1}{K(m^2-1)\pi^2} \left[\frac{1}{(f_m)^{2+\gamma}} - \frac{1}{m^2(f_1)^{2+\gamma}} \right]. \quad (57)$$

If the first and the m -th natural frequencies of the winding are known together with the capacitances C_p and C_s , the parameters of the law (55), K and γ , can be determined by solving the system of (56) and (57).

In reality, the natural frequencies of the winding cannot be measured exactly due to the presence of dissipative phenomena in the winding. These make the resonance frequencies lower than the corresponding natural frequencies (Appendix A.3). In order to minimize the difference between the measured resonance frequencies and the needed natural frequencies, the use of the first and the second resonance frequency in (56) and (57) is advisable. The equation system to be solved, for determining K and γ , becomes then

$$\begin{cases} C_p = \frac{1}{3K} \left[\frac{1}{(f_1)^{2+\gamma}} - \frac{1}{(f_2)^{2+\gamma}} \right] \\ C_s = \frac{1}{3\pi^2 K} \left[\frac{1}{(f_2)^{2+\gamma}} - \frac{1}{4(f_1)^{2+\gamma}} \right] \end{cases} \quad (58)$$

The measurement of resonance frequencies is done by means of the set-ups *a*) and *b*) in Figure 29 respectively.

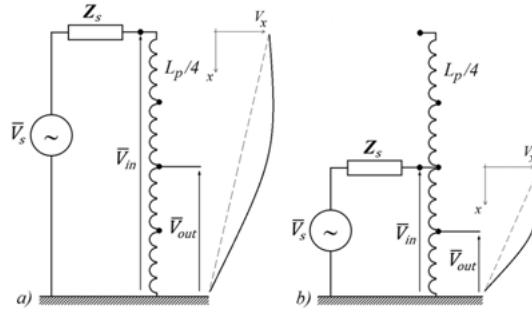


FIGURE 29 – Setups for the detection of a) the 1st and b) the 2nd resonance frequency of the winding respectively (From Paper III).

The first resonance frequency is obtained by supplying the entire field winding and detecting the frequency which maximizes the amplitude of the ratio between \bar{V}_{out} and \bar{V}_{in} at the central tap. The second resonance frequency is detected by supplying the second half of the winding and observing when the amplitude of the ratio between \bar{V}_{out} and \bar{V}_{in} reaches its maximal value at $3/4$ of the winding length. In this second case, if the rotor does not have a number of poles which is multiple of four, it is sufficient to detect the maximum voltage condition at the first available tap close to the $3/4$ of the winding length.

3.3. The simulation in the time-domain

The simulation in the time domain consists in reproducing the voltage responses of the field winding to a fast rising voltage front by using the distributed parameter model presented in Fig. 24. The voltage responses chosen as a reference and to be compared with the results of the simulation are obtained through the setup in Figure 30.

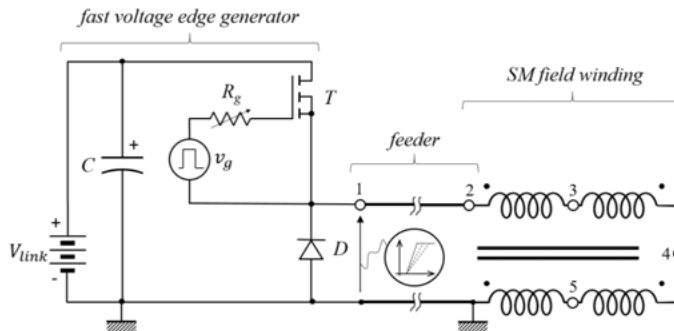


FIGURE 30 – The application of fast rising voltage edges to the field winding through a feeder cable

A generator of fast rising voltage edges, with variable rise time, is applied to the field winding of a four salient pole synchronous machine by means of a bipolar cable (feeder). Considering the field winding initially not excited, when the MOSFET T is switched on, the DC-voltage V_{link} is almost entirely transferred to the field winding. By adjusting the value of the gate resistance, R_g , the risetime of the applied voltage can be varied continuously between 10 ns and 1 μ s. In this way, the cascade of the feeder and the field winding can be supplied with several step voltages showing different rise time.

Moreover, the feeder can be removed so that the fast voltage edge generator directly supplies the field winding.

Since the field winding is a highly inductive load, a flyback-diode is provided in parallel to it. This allows the field current to circulate in the winding for a longer time than the switch-off time of the MOSFET, preventing by that the insurgence of potentially harmful self-induced electromotive forces during the test.

In Fig. 30, five different points (from 1 to 5) are shown, where the voltage responses to a given edge voltage are recorded. These represent the beginning of the feeding cable (point 1) and the four inter-polar taps of the winding (from 2 to 4) respectively. When the feeder is removed, only four winding taps are available for detecting the winding response.

The circuits used for simulating the field winding voltage responses, for the same applied voltages produced by the experimental setup in Fig. 30, are represented in Figure 31 and Figure 32, for the case without and with the feeder respectively.

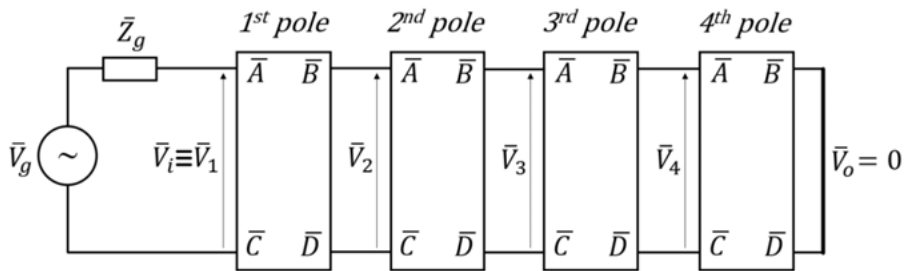


FIGURE 31 – Two-port networks cascade representing the field winding in the frequency domain (from Paper IV).

In both circuits each single pole winding is represented by the same two-port network, the parameters of which,

$$\begin{bmatrix} \bar{A} & \bar{B} \\ \bar{C} & \bar{D} \end{bmatrix} = \begin{bmatrix} \cosh\left(\bar{K}\frac{a}{4}\right) & \bar{Z}_0 \sinh\left(\bar{K}\frac{a}{4}\right) \\ \frac{1}{\bar{Z}_0} \sinh\left(\bar{K}\frac{a}{4}\right) & \cosh\left(\bar{K}\frac{a}{4}\right) \end{bmatrix}, \quad (59)$$

are related to the propagation constant, \bar{K} , and to the characteristic impedance, \bar{Z}_0 , of the single transmission line model in Fig. 24.

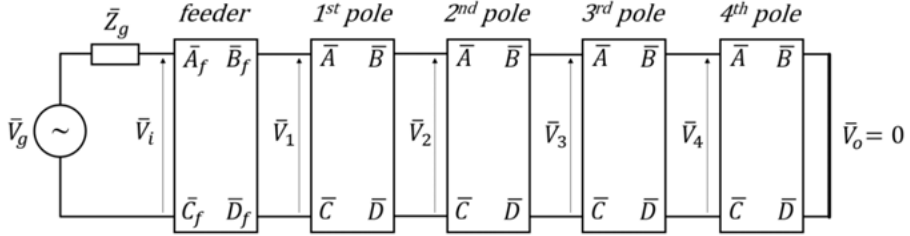


FIGURE 32 – Two-port networks cascade representing the field winding supplied through the feeder in the frequency domain (from Paper IV).

In Fig. 32, a two-port network representing the feeder is set before the cascade of the four pole-winding blocks. The parameters used in this first two-port network are

$$\begin{bmatrix} \bar{A}_f & \bar{B}_f \\ \bar{C}_f & \bar{D}_f \end{bmatrix} = \begin{bmatrix} \cosh(\bar{K}_f a_f) & \bar{Z}_{0,f} \sinh(\bar{K}_f a_f) \\ \frac{1}{\bar{Z}_{0,f}} \sinh(\bar{K}_f a_f) & \cosh(\bar{K}_f a_f) \end{bmatrix}, \quad (60)$$

where \bar{K}_f , $\bar{Z}_{0,f}$ and a_f represent the propagation constant, the characteristic impedance and the length of the feeder respectively.

The generic voltage pulse, provided by the edge voltage generator in Fig. 30, can be represented by the signal shown in Fig. 19b. It has amplitude V , rise time τ and duration $T \gg \tau$, with the spectral density defined by

$$\frac{d\bar{V}_i}{d\omega} = V\tau \left[\frac{\sin\left(\frac{\omega\tau}{2}\right)}{\frac{\omega\tau}{2}} \right]^2 e^{-j\omega\tau} \frac{1-e^{-j\omega(\tau+T)}}{1-e^{-j\omega\tau}}. \quad (61)$$

If $\bar{F}_n(j\omega)$ represents the voltage transfer function at the n -th pole in Fig. 30 for $n=2, 3, 4$, the voltage response to the signal (61) at the same winding tap can be obtained by

$$v_n(t) = \mathfrak{F}^{-1} \left[\bar{F}_n(j\omega) \frac{d\bar{V}_i}{d\omega} \right] = \frac{1}{2\pi} \int_{-\infty}^{+\infty} \bar{F}_n(j\omega) \frac{d\bar{V}_i}{d\omega} e^{j\omega t} d\omega. \quad (62)$$

In the same way, if $\bar{F}_{n,f}(j\omega)$ represents the voltage transfer function at the n -th pole in Fig. 31 for $n=1, 2, 3, 4$, the voltage response to the applied voltage (61) at the same winding tap can be obtained by

$$v_{n,f}(t) = \mathfrak{F}^{-1} \left[\bar{F}_{n,f}(j\omega) \frac{d\bar{V}_i}{d\omega} \right] = \frac{1}{2\pi} \int_{-\infty}^{+\infty} \bar{F}_{n,f}(j\omega) \frac{d\bar{V}_i}{d\omega} e^{j\omega t} d\omega. \quad (63)$$

4. Results and Discussion

The methods presented in the previous chapter have been applied to the three phase, 60 kVA Wound Field Salient Pole Synchronous Machine shown in Figure 33.

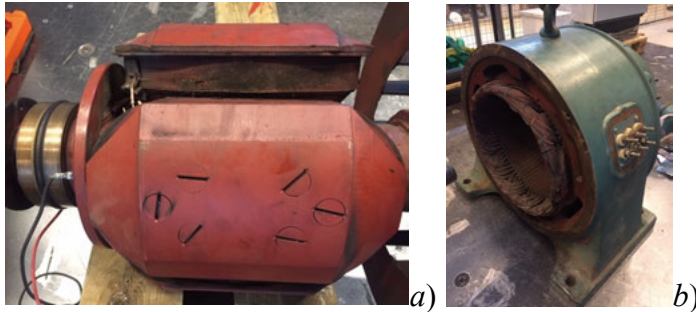


FIGURE 33 – The test synchronous machine: *a)* rotor, *b)* stator.

The main properties of the test machine are summarized in Table 2.

TABLE 2 – Main ratings of the test Synchronous Machine

Rated Power	Rated Voltage	Rated Speed	Pole Pairs	Rated Field Current	Field Winding Resistance (20°C)
S_R (kVA)	V_R (V)	n_R (rpm)	p (-)	I_f (A)	R_f (Ω)
60	400	1500	2	10	6.9

4.1. The parameters of the winding

The parameters of the field winding have been determined by using the methods described in paragraph 3.2. In order to understand the influence of the machine stator on the field winding parameters, these have been measured under two conditions: with the rotor inserted in the stator bore and with the rotor laid outside the stator bore.

4.1.1. The winding capacitances

The determination of the parasitic winding capacitances, according to the capacitive voltage divider method presented in paragraph 3.2.1, has given the results presented in Figure 34 and Figure 35, for the machine frame ground capacitance, C_g , and the winding parallel capacitance, C_p , respectively.

Each measurement has been performed with two different ballast capacitances, C_k (3.2 and 18.3 nF respectively), in order to check the presence of a possible scale factor. The values of the ballast capacitances have been measured through an electronic Q-meter. Fig. 34 shows that the frame capacitance of the machine depends consistently on frequency (~ 7.5 pF/kHz), probably due to the effect of the large conductive surfaces, upon which the displacement current acts. When the rotor is inserted in the stator bore and the stator and rotor share the same potential, the capacitance of the metal frame towards the ground increases. This fact can be recognized through the relative position of the related measurements (diamond markers) with respect to the capacitance trend versus the frequency.

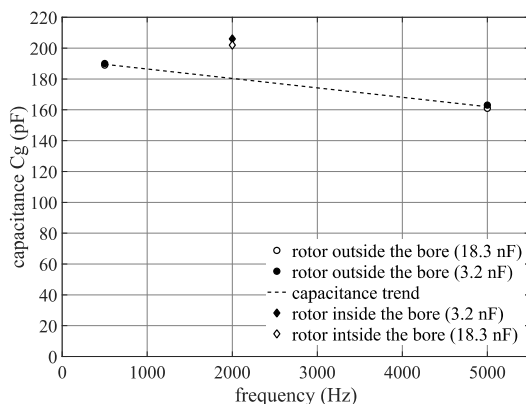


FIGURE 34 – The frame capacitance towards ground.

The capacitance of the winding towards the metal frame, C_p , turns out to be independent from the frequency essentially, how the almost horizontal trend line in Fig. 35 indicates.

It is interesting to observe that the presence of the armature around the rotor does not affect the value of the parallel capacitance. This means that the electrostatic induction of the winding is almost entirely oriented towards the rotor iron and that only a negligible number of field lines crosses the airgap ending up in the stator iron. In other words, the position of the field winding, deeply buried in the spaces between

the poles and enclosed by the polar shoes, makes the electrostatic induction between the winding and the rotor complete.

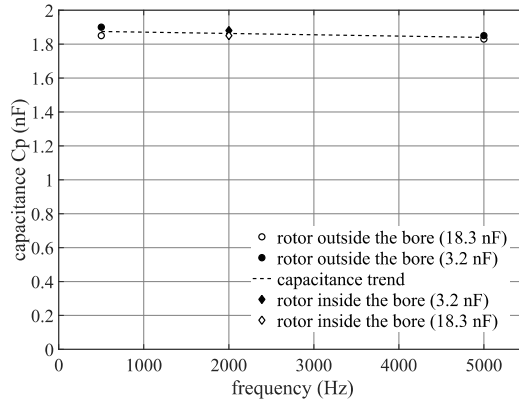


FIGURE 35 – The winding capacitance towards the machine frame.

The parallel capacitance of the winding results in average $C_p = 1.85$ nF, which, referred to the winding length, $a = 1027$ m, gives a specific parallel capacitance of the winding, $c = 1.80$ nF/m.

The determination of the series capacitance of the winding can be done by measuring the specific voltage gradient (36) of the field winding for a frequency larger than the critical one. This permits to find out the ratio (33) between the parallel and the series capacitance, which provides the series capacitance, C_s , once the parallel, C_p , is known.

The markers in Figure 36 show the relative voltage to ground of the winding measured at 230 kHz and at the usual winding taps. The black markers stand for the rotor set into the machine bore and white marker for the rotor outside the machine bore.

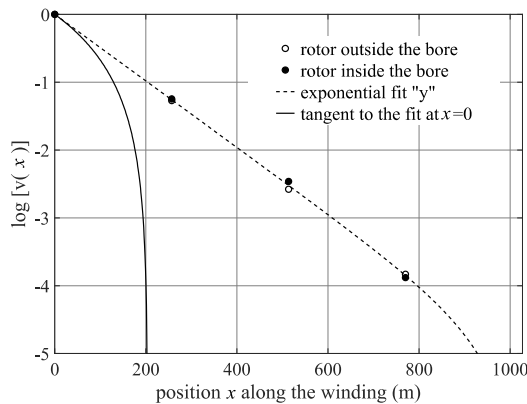


FIGURE 36 – Winding voltage distribution beyond the critical frequency.

It is possible to observe that the voltage measurements are almost the same for the two rotor positions. For this reason, a single common fitting function (46) has been determined, which plots the shaded line in Fig. 36. This fitting curve has a tangent at $x=0$, which is represented by the continuous black curve bending down vertically. This curve tends to the intercept, $a^*=204$ m, on the abscises axis, when the relative voltage tends to zero. Therefore, according to (45) and (48)

$$\frac{c_p}{c_s} = (K_\infty a)^2 = \left(\frac{a}{a^*}\right)^2 = 25.3. \quad (64)$$

From (64), it is possible to conclude that the specific series capacitance of the winding is 25.3 times smaller than C_p , so that the specific winding elastance is

$$k = \frac{1}{c_s a} = \frac{25.3}{c_p a} = 5.4 \mu\text{F}^{-1}\text{m}^{-1}. \quad (65)$$

The possibility to calculate the ratio between the parasitic capacitances of the winding by the specific voltage gradient of the field winding makes it clear, that exactly the ratio between C_p and C_s is responsible for the gradients between the first turns of the winding, when a rapid voltage transients happens. With N being the number of turns in one pole, V_p the DC-voltage applied to the pole and d the distance between two adjacent turns, the maximal electric field due to the rapid transient voltage is

$$E_{max} = \frac{V_p}{N} \frac{1}{d} \sqrt{\frac{C_p}{C_s}}. \quad (66)$$

In Table 3, the values of (66) are estimated with reference to the test machine in Fig. 33 and two further salient pole WFSM machines with rated power 110 kVA and 10 MVA respectively (Figures 37b and 37c).

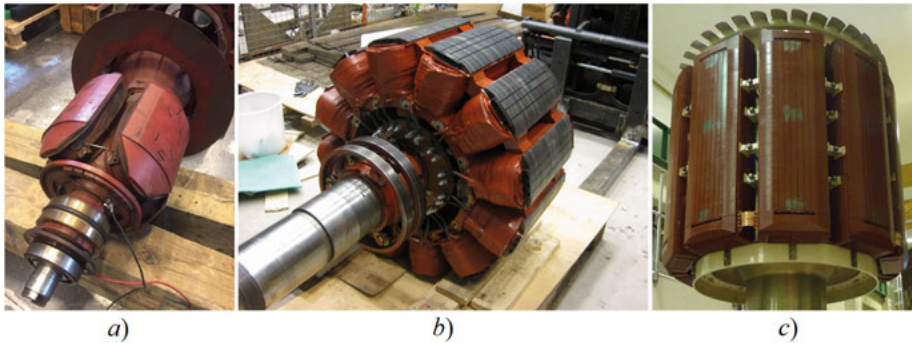


FIGURE 37 – Reference rotors for the voltage gradient estimate: a) $S=60$ kVA, $p=2$; b) 110 kVA, $p=6$; c) 10 MVA, $p=5$.

The maximal electric field is evaluated under three different conditions: A) the field winding is supplied by the nominal field voltage $V_{f,R}$, B) each couple of pole windings are supplied by 325 V_{DC}-link and C) each

couple of pole windings are supplied by 565 V_{DC}-link. The last two conditions refer to the worst-case scenario for the split rotor technique [10], where the DC-link voltage levels achievable from a 400 V-50 Hz network are applied to a pole-pair winding.

TABLE 3 – Estimates of the maximal electric field due to rapid voltage edges.

S_R kVA	p -	$V_{f,R}$ V	a m	d mm	C_p nF	C_s pF	N -	E_{max}^A Vmm ⁻¹	E_{max}^B Vmm ⁻¹	E_{max}^C Vmm ⁻¹
60	2	100	1027	0.05	1.81	71.4	460	5.46	35.6	61.8
110	6	140	1637	0.18	3.60	14.7	162	6.26	87	151
10 ⁴	5	40	924	0.2	36.9	125.8	24	14.3	580	1007

The effect of potential overshoots on the V_{DC}-link has not been taken into account in calculating the voltage gradients of Table 3. According to Table 1, the overshoot could magnify the maximal electric field up to 2.5 times the estimated values. Nevertheless, *it is clear, that the fast voltage edges produced by the power electronics deserve attention in large and slow synchronous machines, when the field current is controlled separately on single poles or on pole pairs, without using an adjustable DC-link voltage.*

4.1.2. The winding resistance

The setup presented in paragraph 3.2.2 has permitted the indirect measurement of the parallel resistance R_p of the field winding under the two conditions, rotor put inside and outside the stator bore respectively. In order to target different parallel resonance frequencies in the winding a set of six different ballast capacitances, C_k , has been used. Figure 38 shows the results of the measurements.

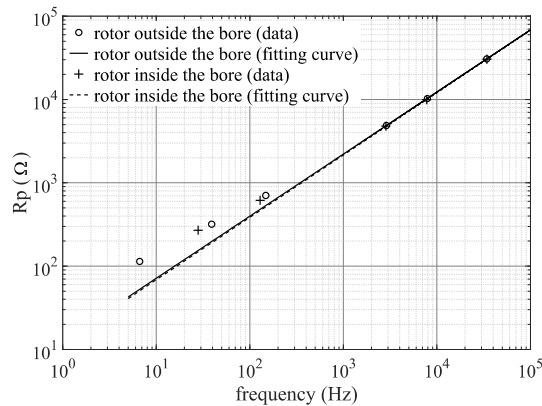


FIGURE 38 – The trend of the parallel resistance of the winding (From Paper III).

The first fact to recognize in Fig. 38 is that *the presence of the stator around the rotor does not affect the dependency of the parallel resistance on the frequency*. In fact both set of markers (circles for the rotor outside and crosses for the rotor inside the bore) follow the same trend in frequency. This result has been theoretically anticipated in Paper II, where it is shown that the parallel resistance model is to be preferred to the series resistance one for representing the eddy current losses in the field winding. This is due to its independence from the armature reaction and the airgap dimensions. The second remark is about the trend of the resistance law at higher frequency. In the kHz range the measured values show a constant trend, which is caught very well by (53). The fit of the data by (53) has revealed that the parallel resistance grows with the power 0.7 of the frequency. Since the resistance R_p is related to the eddy currents in the rotor iron mainly, its dependence on frequency should theoretically point to the power 0.5 (Paper II). The discrepancy between the expected result and the one obtained is probably due to the ability of the chosen experimental approach to capture second order dissipative phenomena in the winding, which were not foreseen or conceptually modeled in advance. This stresses even more the importance of an experimentally based approach for building a frequency dependent model of the field winding.

4.1.3. *The winding inductance*

The determination of the field winding inductance law needs the measurements of the first and second resonance frequencies of the winding in advance (paragraph 3.2.3).

This is done by means of the setups in Fig. 29a and Fig. 29b and the results are presented in Figure 39 and 40 respectively.

Fig. 39 shows that the voltage transfer function at the central tap of the winding is essentially the same for the rotor laying outside the machine bore or inside it. The peak of the transfer function is reached at 43.4 kHz and it represents the first resonance frequency of the winding.

By supplying the second half of the winding and measuring the output voltage at $\frac{3}{4}$ of the winding length, the voltage transfer functions in Fig. 40 are obtained. Contrarily to Fig. 39, the relative position of the rotor and the stator makes a difference between the transfer functions in Fig. 40. It is clearly recognizable that the second resonance frequency is higher when the rotor is set into the stator bore (74.32 kHz) than when the rotor is completely extracted from the machine (71.11 kHz).

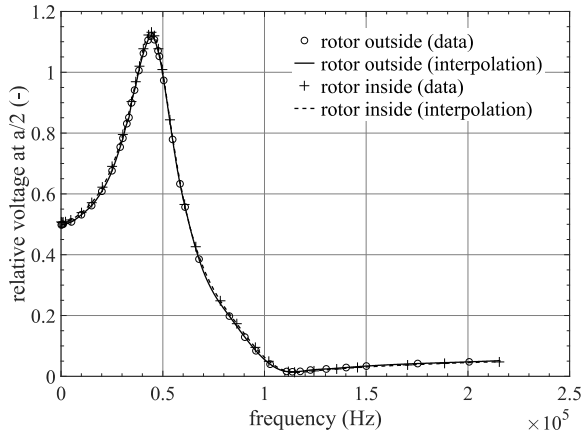


FIGURE 39 – The detection of the first resonance frequency of the field winding earthed at its end (from Paper III).

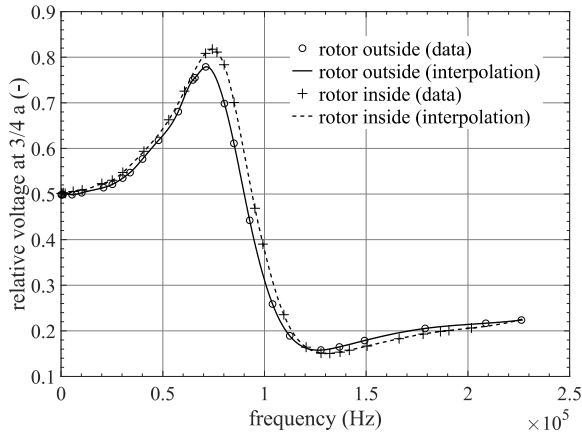


FIGURE 40 – The detection of the second resonance frequency of the field winding earthed at its end (from Paper III).

Since the measurement of the winding parasitic capacitances has proved that these are not affected by the presence of the stator around the rotor (paragraph 4.1.1), according to (44), the change of the 2nd resonance frequency in the winding depends on a change in the winding inductance. The equation system in (58) finds out the inductance law of the winding, once the parasitic capacitances, C_p and C_s , are known together with the first and second resonance frequencies. In Figure 41, the inductance law determined through (58) is reproduced for the rotor set into the machine bore (dashed line) and for the rotor outside it (continuous line).

Both curves plotted in Fig. 41 show that *an increasing frequency produces a drop in the inductance value*. This is in line with the results of Paper II, which represents the winding inductance as negatively correlated to the frequency, due to the demagnetizing effect of the eddy currents.

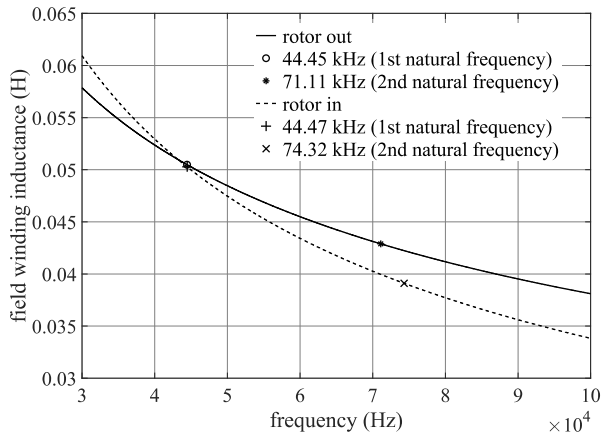


FIGURE 41 – The test synchronous machine: *a*) rotor, *b*) stator (from Paper III).

It is by chance that the two curves cross each other exactly at the first resonance frequency, because there is not physical reason why these should. Nevertheless, below the first resonance frequency the presence of the armature around the rotor makes the field winding inductance higher than in the case of the rotor alone. This can be explained by the lower reluctance path for the field winding magnetic flux, when the rotor is inside the bore. At higher frequencies than the first resonance one, *the degaussing effect of the eddy currents is strengthened by the presence of the armature and it results in a steeper decrease of the winding inductance versus the increasing frequency*. This evidence is very counterintuitive since it shows that the presence of a ferromagnetic and conductive closure path for the flux does not always contribute to an increase of the inductance for the exciting winding. In cases like the one presented in Fig. 41, the improved reluctance path for the flux reinforces the demagnetizing effect of the eddy currents more than the flux itself. Since the inductance of the field winding is reduced by the presence of the stator for frequencies in the kilohertz range, it is possible to foresee that high frequency voltage waves propagate faster in the winding when the rotor is inserted into the machine bore rather than outside of it. *This fact makes the field winding appear “electrically shorter” when the rotor is inside the stator bore*. For this reason, *the overvoltage*

test to rapid voltage edges, performed on the winding of the sole rotor, must be considered harsher than the one performed on the finally assembled machine.

The inductance laws represented in Fig. 41 have been measured without paying attention to the angular position between rotor and stator, which could play a role in changing the inductance value when the rotor is inserted in the stator bore. Potential influences in that sense can be exerted, e.g., by the armature slotting and by the rotor eccentricity. In Paper III an experimental setup and procedure have been specifically proposed for detecting an eventual variation of the winding inductance or of the winding parasitic capacitances, due to the rotor angular position. This technique is based on the detection of a phase displacement between the voltage at the beginning and at the end of the winding closed on a resistor, under the condition that the voltage is tuned on $\frac{3}{4}$ of the winding length (Figure 42a). Fig. 42b does not shows relative displacements between the two measured voltages, in spite of the different rotor angular positions. This means that no changes intervene in l , c or k , since the winding wave number (29), which depends on l , c or k , has remained unaffected.

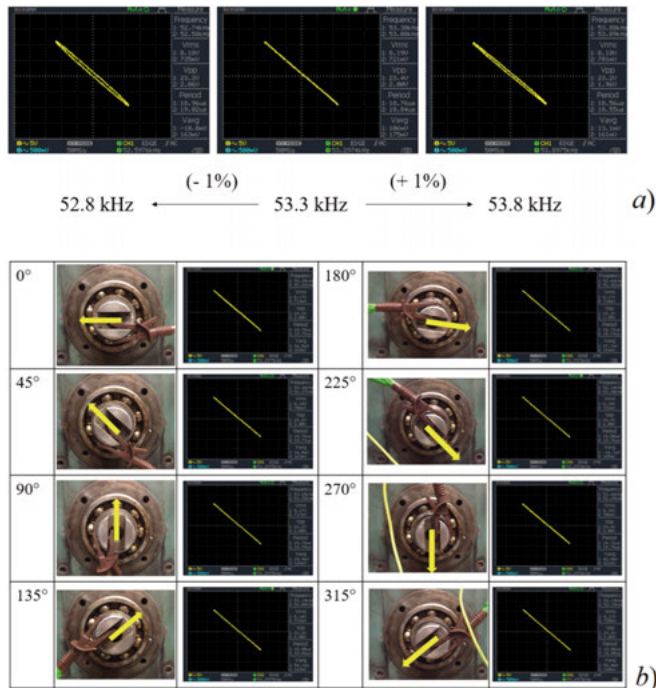


FIGURE 42 – XY-mode for detecting a voltage phase shift due to a) a frequency variation, b) a change in the inductance/capacitance of the winding (from Paper III).

4.2. The frequency response of the winding

Once the determination of the parameters for the model in Fig. 15 is completed, the transfer function (26) can be compared with the transfer function of the winding detected at the usual winding taps. Since the propagation constant of the winding \bar{K} depends on the frequency, three different frequencies have been chosen for reproducing the voltage profile. These frequencies are representative of three different behaviors of the field winding: a subcritical behavior at low frequency, a subcritical behavior at the first resonance frequency and a supercritical behavior (beyond the winding resonance frequencies).

Figure 43 shows the voltage distributions of the winding earthed at its end for the case of the rotor outside the stator bore. Figure 44 represents the same profiles for the rotor inserted in the stator bore.

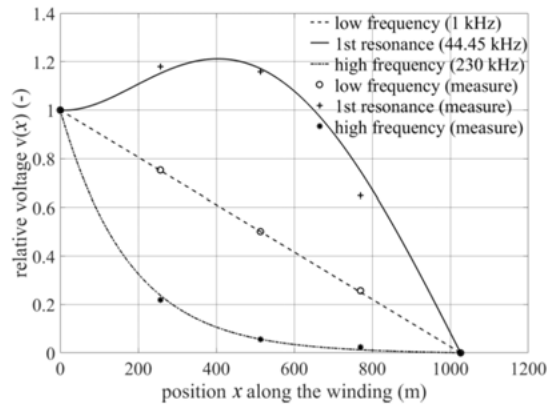


FIGURE 43 – Voltage profiles for the rotor outside the stator bore (from Paper III).

In both cases, it can be observed how close the adopted model in Fig. 15 can reproduce the real voltage profiles for the chosen frequencies.

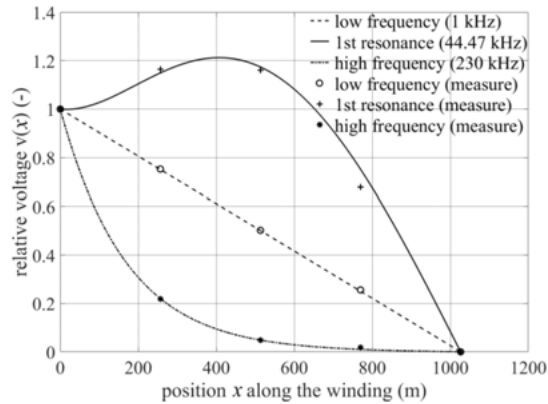


FIGURE 44 – Voltage profiles for the rotor inside the stator bore (from Paper III).

At 1 kHz the inductive reactance is the parameter determining the linear distribution of the voltage along the winding. At the first resonance frequency (around 44 kHz) the voltage profile is not linear anymore due to the dynamic emphasis of the resonance itself. The transfer function reaches its highest value close to the middle point of the winding. This value is related to the quality factor Q_I of the winding. In both figures Q_I can be estimated by the voltage amplification at $x=a/2$, which is circa 2.4. The damping factor ζ_I of the winding at the first resonance frequency is then

$$\zeta_1 = \frac{1}{2Q_1} \cong 0.21. \quad (67)$$

From Fig. 40 the quality factor for the second resonance frequency is $Q_2 \cong 1.6$. The correspondent damping factor is then

$$\zeta_2 = \frac{1}{2Q_2} \cong 0.31. \quad (68)$$

The comparison between (67) and (68) shows that the winding losses increase rapidly with the order of the resonance frequency.

Once the frequency of the voltage applied to the winding overcomes the critical frequency (95.8 kHz for the rotor outside and 103.2 kHz for the rotor inside the stator bore respectively), the resonance is not possible anymore and the capacitive behavior of the winding sets the voltage profile distribution. For the chosen frequency 230 kHz, which is more than twice as larger as the critical frequency, the voltage profile can be assumed as that for $f \rightarrow \infty$. Therefore, for frequencies higher than 230 kHz the voltage distribution is defined entirely by C_p and C_s and remains exactly the same as measured at 230 kHz. It can be concluded that starting from 1 kHz, up to frequencies beyond 230 kHz, the suggested single transmission line model shows to correctly describe the frequency behavior of the field winding.

4.3. The time domain simulation

The good frequency response of the winding model (paragraph 4.2) over a wide frequency range makes it eligible for reproducing the winding responses to different applied voltages in the time domain. Therefore, Paper IV has been concerned with the use of the same model for achieving timely voltage responses at the usual winding taps. Three different tests have been done. In the first test the field winding is supplied with an AC triangular wave at low frequency. This test must explore

how the model works in steady state. In the second test a rapid rising voltage edge produced by the generator in Fig. 30 is applied at the winding terminals directly, in order to excite the free response of the winding. In the last test, the same generator of fast voltage edges is connected to the field winding by means of a bipolar cable (feeder). In this way, by choosing the feeder length opportunely, it is possible to cause over-voltages into the winding with supercritical frequency.

4.3.1. *The steady state simulation*

Figure 45 shows the real tap voltages (continuous plots) produced in the winding by a triangular AC supplying voltage of amplitude 7.5 V and frequency 12.3 kHz, which is directly applied at the winding terminals. It can be observed that the voltage amplitude decays linearly along the winding and that the peak voltage is more delayed, the farther is the winding tap from the winding starting point. Moreover, the comparison of the tap voltages with the supply one shows the distortion introduced by the winding.

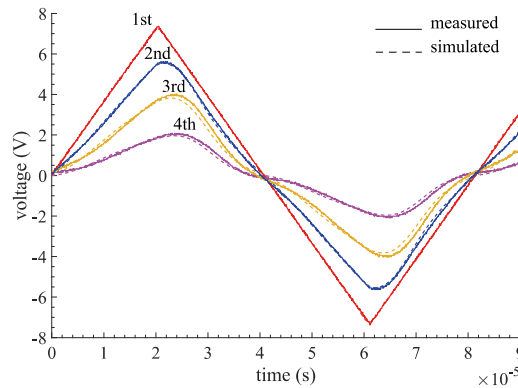


FIGURE 45 – Comparison between the measured and the simulated response voltages at the interconnections between the pole windings, as represented in Fig. 31. Input voltage applied to the winding directly: amplitude 13 V, frequency 12.3 kHz. (from Paper IV).

The input voltage for the simulation includes frequencies until the 12th harmonic (147.6 kHz) and it can be observed how good the model reproduces the tap voltages (shaded plots). Figure 46 shows the results of the same simulation where the input voltage includes the harmonics till the fifth one (61.5 kHz) only. Comparing Fig. 45 and Fig. 46, the only visible difference is about the input voltage. The filtering effect of the winding is so strong after just one fourth of the winding length, that the

harmonics of the input voltage beyond the 5th do not play practically any role in the voltage responses.

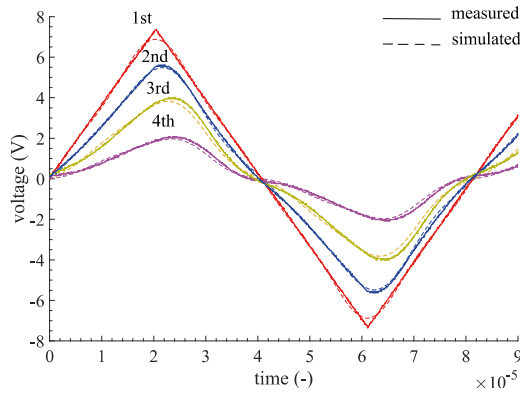


FIGURE 46 – Comparison between the measured and the simulated response voltages at the interconnections between the pole windings, as in Fig. 31. The input voltage for the simulation only considers the harmonics up to the 5th order (from Paper IV).

4.3.2. *The subcritical behavior*

Figure 47 shows the tap voltages produced in the winding by a positive sloped voltage edge with amplitude 13 V and rise time 0.2 μ s. The rapid voltage front is applied to the winding terminals directly. The continuous plots represent the actual tap voltages whereas the shaded ones stand for the simulated voltages.

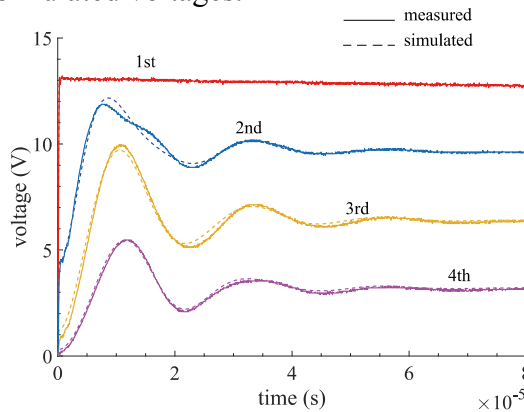


FIGURE 47 – Comparison between the measured and the simulated response voltages at the interconnections between the pole windings, as represented in Fig.32. Input voltage applied at the winding directly: rising voltage edge 13 V, rise time 0.2 μ s (from Paper IV).

It must be observed that the pseudo-periodic ringing, triggered in the winding by the rapid voltage edge, has a frequency of 44 kHz, which is practically coincident with the first resonance frequency detected in Fig. 39. Therefore, that ringing is the result of the superposition of a progressive and a regressive voltage wave at the first natural frequency essentially, which builds up a standing-wave-like voltage distribution in the winding. In fact, the largest overshoot of the voltage happens in the middle of the winding, whereas the overshoots at $\frac{1}{4}$ and $\frac{3}{4}$ of the winding length are smaller and equal in amplitude. At the beginning and at the end of the winding there are voltage nodes of course, since the voltage is fixed there. The rapid voltage edge applied to the winding causes more natural voltage waves other than the first order one to travel and to superpose in the winding. However, since these undergo a stronger attenuation than the first natural one, the ringing is essentially defined by the first natural frequency. In conclusion, the natural free response of the winding to a step-like voltage evokes only the natural frequencies of the winding, which are all subcritical. The part of the input spectrum exceeding the winding critical frequency cannot be propagated into the winding in form of a wave, since the critical frequency is the ultimate propagation mode. Therefore, it is reflected back to the generator and get dissipated on the internal generator resistance. From this point of view the voltage generator represents a strong voltage source and this is the reason why it can force the voltage at the winding terminals.

4.3.3. *The supercritical behavior*

Figure 48 presents the voltage response of the field winding to a rapid voltage edge, when the winding is supplied through a 19 m long bipolar cable.

In this test the stationary voltage level is 6.5 V and the rise time 50 ns. The ringing produced by the test has a pseudo-frequency of 1.33 MHz, well beyond the critical frequency of the winding, which is circa 96 kHz. This remark excludes that the ringing can be sustained by voltage waves related to the winding natural frequencies. Therefore, the origin of the observed overvoltages is external to the winding and depends on the feeder. In Paper IV, it is shown that the frequency of the ringing can be related to the properties of the cable essentially. Nevertheless, it can be observed in Fig. 48, that the supercritical overshoots can be detected not only at the terminals of the winding but all along it. The mechanism for transferring the supercritical perturbation from the beginning of the winding to its end is based on the electrostatic induc-

tion, since the supercritical nature of the winding is definitively capacitive. This is confirmed by the real nature of the propagation constant (33), which produces only attenuation of the overshoots along the winding without introducing any phase shift between them. In Fig. 48, it is possible to recognize that the relative maxima of the overshoots almost happen at the same time at different taps of the winding and so do the minima. Moreover, the decay of the voltage overshoot amplitude resembles the pseudo-exponential voltage distribution observed in the winding (Figures 25, 43 and 44) for supercritical frequencies.

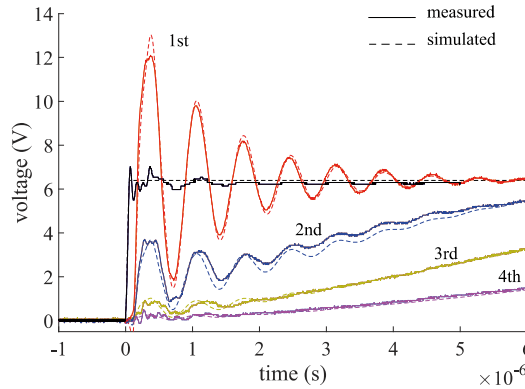


FIGURE 48 – Comparison between the measured and the simulated response voltages at the interconnections between the pole windings, as represented in Fig. 32. Input voltage applied through the feeder: rising voltage edge of 6.5 V with rise time 50 ns. (from Paper IV).

Considering the mechanism of generation of the overshoots, one classical way to explain it points to the mismatch between the characteristic impedance of the cable, $\bar{Z}_{0,f}$, and the input impedance, \bar{Z}_i , of the field winding [37]

$$\hat{V}_1 = \left\| \frac{2\bar{Z}_i}{\bar{Z}_i + \bar{Z}_{0,f}} \right\| \hat{V}_{in}. \quad (69)$$

However, the frequency dependence of (69) makes it not suitable for getting a plain explanation of the phenomenon in the time domain. Furthermore, it does not point directly to the voltage edge features in order to explaining the generation of the ringing. A more convenient way to do this is by following the theory of travelling waves applied to the transformer windings by R. Rüdberg [38].

A rising step voltage $u(t) \cdot V$ can be regarded as the sum of the DC-term with amplitude $V/2$ and the odd sign function $sgn(x)$ multiplied by $V/2$. The sign function is knowingly related to the edge of the step voltage. Moreover, its Fourier transform is

$$\mathfrak{F}\left[\frac{V}{2} \cdot sgn(x)\right] = \frac{V}{2} \left[\frac{2}{j\omega} \right] = \frac{V}{j\omega}. \quad (70)$$

The part $v_c(t)$ of the step voltage, $u(t) \cdot V$, which can penetrate the winding is related to all signal harmonics which are subcritical. According to (68), it can be expressed as

$$v_c(t) = \frac{V}{2} + \frac{1}{2\pi} \int_{-\omega_c}^{+\omega_c} \frac{V}{j\omega} e^{j\omega t} d\omega = \frac{V}{2} + \frac{V}{\pi} \int_0^{+\omega_c} \frac{\sin(\omega t)}{\omega} d\omega, \quad (71)$$

since (70) is an odd function in $j\omega$. The integral term of (71) is called integral sine, briefly $Si(\omega_c t)$, so that the normalized form of the function $v_c(t)$ can be written as

$$v_{c,n}(\xi) = \frac{v_c(\xi)}{V} = \frac{1}{2} + \frac{1}{\pi} Si(2\pi\xi), \quad (72)$$

where

$$\xi = \frac{2\pi t}{\omega_c} = \frac{t}{T_c}. \quad (73)$$

The function (72) is represented in Figure 49 and shows that the part of the indicial input voltage, which can completely penetrate a field winding with the critical frequency f_c , is a step signal with the rise time not larger than half the critical period T_c . The voltage edge which shows the ultimate rise time $T_c/2$ can be called critical voltage edge.

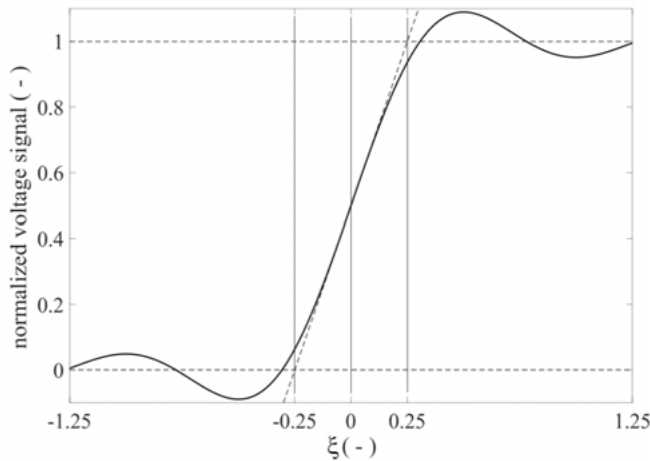


FIGURE 49 – The normalized critical voltage edge (from Paper IV).

Therefore, as soon as the rise time of the voltage edge applied to the field winding is shorter than half the winding critical period T_c (supercritical voltage edge), the difference between the applied and the critical signal, Δv_i , gets rejected by the winding and reflects back towards the feeder. Figure 50a shows a step voltage, a critical voltage edge and a supercritical voltage edge, whereas Figure 50b shows the respective generated voltage residuals Δv_i .

From Fig. 50b, it results that, beyond the critical rise time, the steeper the voltage edge, the higher the amplitude of the voltage residual getting reflected back to the supplying line. This fact poses a straightforward correlation between the amplitude of the first overshoot at the winding

terminals and the rise time of the applied voltage edge. In that sense, this approach to the ringing mechanism in the time domain explains the overshoots generation, by comparing the voltage edge rise time with a characteristic time T_c of the field winding.

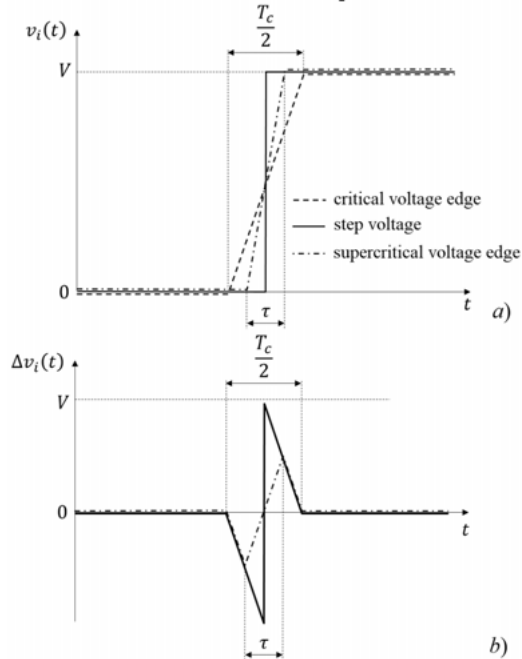


FIGURE 50 – a) Three different voltage edges, b) their relative voltage residuals.

The validity of this conclusion has been experimentally tested by means of the setup in Fig. 30. Figure 51 shows the field winding responses recorded at the winding terminals for four different voltage edges applied at the beginning of the feeding cable.

Since the field winding has a critical frequency of ca. 96 kHz, the critical rise time corresponds to ca. 5.2 μ s. In Fig. 51, the progressive increase of the rise time from the supercritical value, in Fig. 51a, to the subcritical one, in Fig. 51d, significantly reduces the amplitude of the voltage overshoots. In particular, for the subcritical voltage edge in Fig. 51d, the ringing disappears completely. According to Fig. 50b, the maximal relative overvoltage can reach twice the steady state voltage of the step signal, when the rise time is zero. In Fig. 51, the input voltage to the feeder does not remain constant but resonates of the inductive nature of the electrolytic capacitor connected to the DC-link in the setup in Fig. 30. For this reason, some voltage overshoots can be observed at the beginning of the feeder too, when the voltage edge is supercritical. Nevertheless, the ratio between the overvoltage at the termination of the feeder and the correspondent overvoltage at the beginning of the feeder (transmission coefficient) does not exceed two. *This fact highlights that,*

if the DC-link voltage is not properly stabilized by a large low inductive capacitor, the overvoltage triggered by supercritical voltage edges at the end of the feeding cable could exceed twice the steady-state voltage.

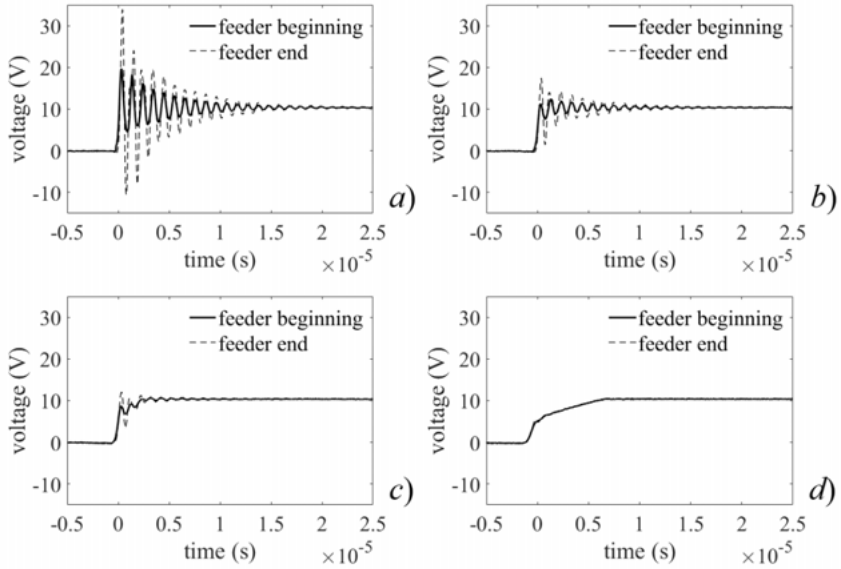


FIGURE 51 – The field winding voltage response at the winding terminals and a the beginning of the feeder for different rise times of the voltage edges: *a)* 0.29 μs , *b)* 0.35 μs , *c)* 1.50 μs , *d)* 5.38 μs (from Paper IV).

5. Main outcomes of this work

5.1. Relevant parameters for modeling the field winding and the feeder

The model for the field winding proposed in Paper III and that for the feeding cable used in Paper IV have proved to be capable of reproducing the voltage to ground along the winding for subcritical and supercritical frequencies (Fig. 43 and 44) and for subcritical and supercritical signal voltage edges (Fig. 45, Fig. 47 and Fig. 48). Therefore, the present paragraph recalls and summarizes all the evidences gathered about the model parameters through the experimental work.

5.1.1. *The field winding parameters*

The specific parallel resistance, r_p , (Fig. 38) and the specific inductance, l , (Fig. 41) of the field winding depend strongly on the frequency. A STLM, which must reproduce the behavior of the winding over a wide range of frequency, cannot assume the two parameters as constant. Unfortunately, the experimental determination of the frequency laws for both parameters shows correlations with the frequency which differ from the theoretical ones (Paper II vs Paper III). For this reason, it is not possible to presume the frequency laws for those two parameters a priori. Two possible reasons could explain this discrepancy:

- a) more complicated EM second order effects get caught and summarized by the parameters of the model, well beyond the goal they were meant for;
- b) the modeling of the field winding is too simple and additional parameters should be introduced for accounting those differences.

Nevertheless, the model gives good results and has the advantage to be very simple.

During the modeling of the field winding, the specific parallel resistance (fig. 10b) has been preferred to the specific series resistance of the winding (Fig. 10a), for reproducing the losses related to the eddy currents. The parallel resistance has the advantage to be independent from the armature reaction and from the mechanical irregularity of the airgap. This feature of r_p , which has been foreseen in Paper II, is confirmed by the experimental work of Paper III (Fig. 38). In fact, the frequency law of the field winding parallel resistance does not change essentially if the rotor is inserted into the machine bore or not. This evidence has been tested on a solid salient pole SM starting from the frequency of 7 Hz, where the eddy current reaction in the rotor begins already at very low frequency. It is possible to expect that, in the case of a laminated magnetic circuit of the rotor, this kind of insensitivity to the armature presence would start from the frequency where the iron is not fully penetrated anymore. Just for reference, an almost saturated ($\mu_r=10$) iron lamination, 0.35 mm thick becomes partially penetrated (95%) starting from circa 3.2 kHz.

With reference to the specific inductance, l , it has been observed that the presence of the armature around the rotor influences its frequency law. In particular the decay of the inductance versus the frequency is steeper when the rotor lies in the machine bore rather than outside it. Therefore, in order to determine the frequency law of l , it is necessary to perform the measurements described in paragraph 3.2.3 with the rotor inserted in the stator bore.

A specific test has checked if the angular rotor position can possibly affect the value of the specific field winding inductance. The results, shown in Fig. 42, do not reveal this kind of effect. However, it must be observed that the test machine in Fig. 33 has a one tooth-pitch skewed stator slotting and that, again, it presents solid salient poles. The first characteristic neutralizes the inhomogeneity of the airgap due to the stator slots, whereas the second one makes the machine airgap virtually larger due to the demagnetizing effect of the eddy currents. This last aspect reduces drastically the effect of eventual rotor eccentricity or stator ovality on the value of the specific field winding inductance.

The specific parasitic capacitances of the field winding, c_p and c_s , have been assumed as constants in the model, starting from the evidences of the constancy of c_p versus the frequency. The determination of both parameters requires two experimental steps. The first one determines the winding capacitance, C_p , by means of the voltage divider in the setup in Fig. 26. The second step measures the relative voltage gradient of the winding at high frequency, where the nature of the winding is definitively capacitive.

5.1.2. *The feeder parameters*

The STLM of the bipolar cable is a well-known state of the art and it presents four specific parameters only: the AC wire resistance, r_f , the inductance, l_f , the capacitance, c_f , and the conductance of the insulation, g_f . In this model, there is not a prevalent source of losses, as it has been the case for the field winding model (eddy current losses). Therefore, both dissipative parameters, r_f and g_f , must be taken into account. The wire AC-resistance resents of both skin and proximity effect, so that the cable resistance at 100 kHz can assume a value which is several times the DC one. The adoption of a cable with stranded wires reduces this kind of effects. In Paper IV, it is shown how to calculate the frequency law for the specific resistance, r_f , in the case of a bipolar cable with stranded wires.

For determining the specific cable conductance, g_f , there are not calculation approaches available. Therefore, the value of g_f must be either found in the cable specifications or it must be measured. The cable specifications are usually stated for one single frequency, which makes the information useless for finding out a frequency law for g_f . Nevertheless, the effect of the dielectric losses becomes relevant at high frequency so that g_f can be related to the specific cable reactance by means of the dielectric loss angle of its insulating material.

The specific capacitance, c_f , is normally stated in the cable specification. This parameter can be calculated using the cable geometry and the dielectric permittivity of the insulation. In Paper IV, the specific capacitance for a bipolar cable is calculated and measured respectively. The obtained results confirm the validity of the analytical approach.

The specific cable inductance, l_f , is in general a frequency dependent parameter. The part of the inductance depending on the frequency is the internal inductance of the wire essentially, whereas the external contribution to the inductance remains constant. The determination of a frequency law for the feeder inductance is advisable, when it is made of conductive bars of solid wires. When the wire is finely stranded the skin effect and proximity effect become first sensible at very high frequency. For that reason, the specific cable inductance can be considered constant. Once the specific inductance and the specific capacitance of the cable are assumed as constant, it is possible to estimate the frequency of the ringing triggered by fast voltage edges on the field winding. In fact, it depends on the winding length and on the relative permittivity of the cable insulation essentially. The estimation of this frequency is very important, since it permits to assess if the complex formed by the feeder and the winding model are going to work in a supercritical mode. Moreover, the knowledge of the ringing frequency enables estimates about the parameters, r_f and g_f , in advance.

5.2. Measures for reducing the electric stress

The estimates of the maximal voltage gradient in the winding represented in Table 3 show that the fast switching could be problematic for large and slow solid salient pole WFSM, where the current control is performed by “chopping” a relatively high DC-link voltage. This technique is advantageous on the one side because it does not require a step down transformer in the VSC or additional PE for reducing the DC-link voltage. Furthermore, it keeps a relatively high voltage source ready for producing high ceiling voltages or boosting the current dynamic. However, on the other side, it exposes the winding permanently to the highest voltage excursion during the switching. Therefore, in light of the results obtained through this research, this paragraph presents the measures which can reduce the electric stress in the field winding during highly dynamic current control.

5.2.1. *The field winding design*

Equation (66) shows that the electric field between the initial turns of the winding is proportional to the square root of the ratio between the capacitance of the winding towards the rotor frame, C_p , and the series capacitance of the winding, C_s . In terms of relative voltage gradient (36), the winding arrangement in Figure 52a, which presents less capacitance towards the iron frame (thicker insulation) and higher turn to turn capacitance (smaller distance between the turns), is less critical than the one if Fig. 52b.

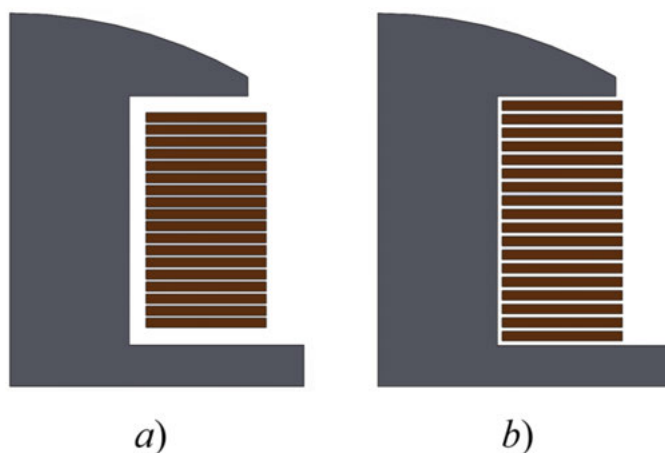


FIGURE 52 – Different field winding arrangements: a) low C_p and high C_s ; b) high C_p and low C_s .

However, since the thickness of the non-functional insulation towards the rotor frame has a limit due to mechanical reasons, the capacitance C_p can be considered constant in (66). This implies that the maximal electric field established between the first turns of the winding during a fast voltage edge gets reduced by increasing the turn-to-turn distance, d . Nevertheless, under the condition of constant C_p , the same electric field decreases very slowly when the turn-to-turn distance increases, as the following simple derivation from (65) shows

$$E_{max} \approx \frac{V_p}{N\sqrt{d}} \quad (73)$$

A possible solution for mitigating the high voltage gradient affecting the initial turns of the winding, without changing the underlying design of the insulation, is that suggested by the design of high voltage transformers [39]. Figure 53 shows some metallic electrostatic shields laid down on the lateral insulation of the first three-to-four turns of the pole winding. If these shields are kept insulated from the rotor frame, they increase the specific turn-to-turn capacitance, $\propto C_s$, in the first portion of the winding, without contributing to the capacitance C_p .

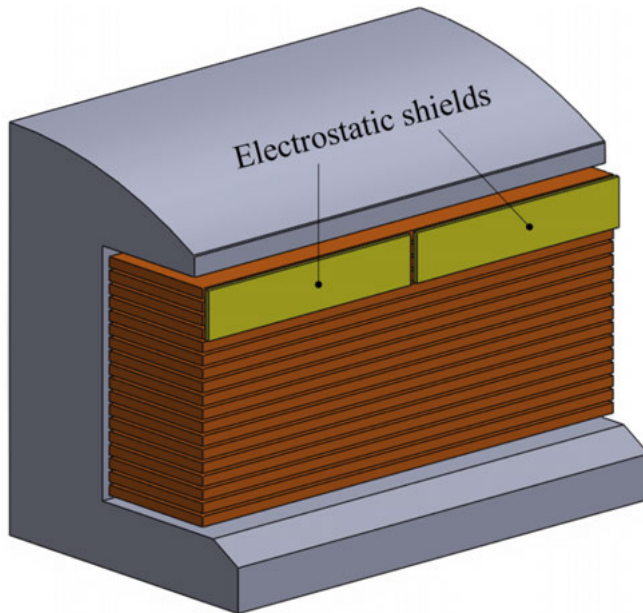


FIGURE 53 – Electrostatic shields for reducing the voltage gradient on the first turns of the winding during rapid variations of the supplying voltage.

The field winding with a multilayer structure is frequently used in small size synchronous machines. Moreover, due to the relatively high number of turns that it uses, it is not suitable for high dynamic field current control applications. Nevertheless, it can be recognized from Figure 54

that the parasitic capacitances existing between the layers, while reducing the capacitance towards the rotor frame of the more external layers, increase the turn-to-turn capacitance.

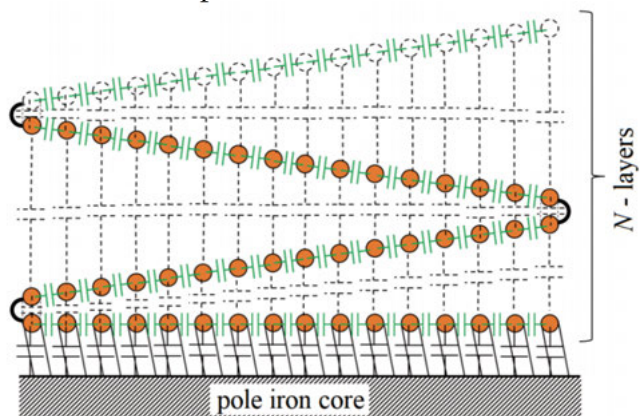


FIGURE 54 – The contribution of the inter-layer electrostatic induction to the turn-to-turn capacitance.

Therefore, where this field winding arrangement can be used, it takes advantage from the naturally favorable C_p/C_s ratio.

5.2.2. The reduction of the voltage slew rate

In Fig. 50, an explanation for the generation of the voltage overshoots at the termination of a supplying cable has been given, which is alternative to the mismatch of the feeder and winding impedances. That explanation points to the extension of the rise time of the voltage edge as one measure for reducing the amplitude of the voltage overshoots at the field winding terminals. Figure 55 (Paper IV) shows the relative amplitude of the overshoot to the DC-link voltage for different relative values χ of the rise time to the critical one.

The longer the rise time the smaller the overshoot amplitude, till to the point that, for a rise time which equals or exceeds half the critical period of the winding, the overshoots disappear completely.

Slowing down the commutation process of the switches by controlling the gate voltage can be an option when the commutation frequency is very low and the timely crossing of commutation current and commutation voltage does not generate too large switching losses. Alternatively, the commutation current can be reduced by using snubber-circuits, so that the switching losses are partially shifted from the switch itself to the relative snubber. However, due to the fact that the capacitors are always critical components in a circuit (due to the potential break-

down), this kind of application is not advisable for generation systems where the reliability is a key requirement.

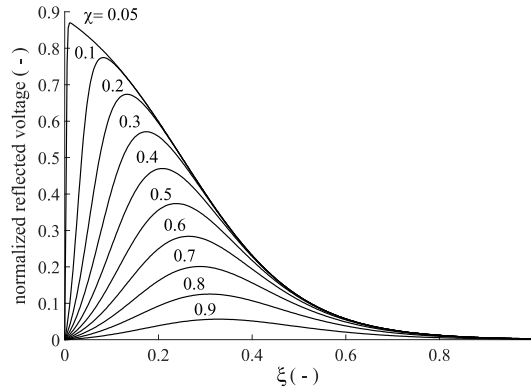


FIGURE 55 – Intensity χ and relative position ξ of the voltage overshoot.

A generic schematic for a PE supplied split rotor field winding is shown in Figure 56. The schematic considers the split rotor winding since it is more flexible in terms of potential applications than a traditional one. Moreover, it requires a more complex PE, due to its polyphase structure. In this sense, Fig. 56 resembles a generic drives topology for an AC-machine. According to this, low pass filters or impedance-adapting boxes can be used close to the PE or close to the field winding respectively, in order to reduce or preventing voltage overshoots [40].

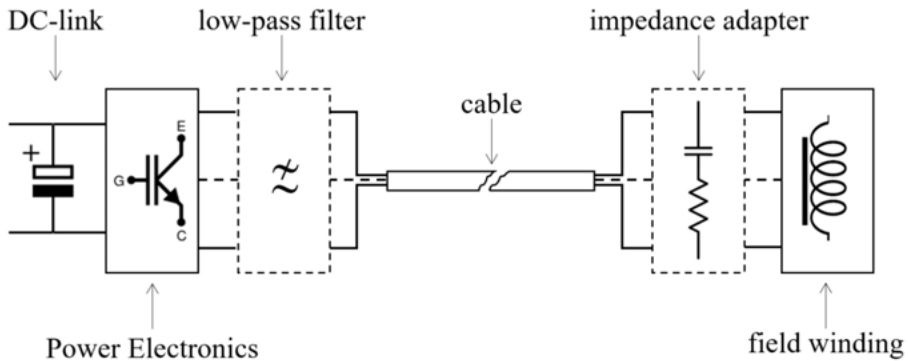


FIGURE 56 – Where to insert the low-pass filter and the impedance-adapter in the supply cascade of a split-rotor field winding.

The impedance adapter is a very simple device. It must contain an RC filter which presents the admittance $1/R_{of}$ beyond the winding critical frequency, otherwise as low as possible. However, a capacitor placed in that position represents an additional failure risk for the system.

For that reason, practical solutions must consider inductive low-pass filters without capacitors to be placed close to the PE. An inductive low pass filter presents a transformer-like structure and it is also known as dV/dt-filter. In Figure 57 an alternative picture of the schematic in Fig. 56 is given, where, the filter, the feeder and the field winding are represented in more detail. For simplicity, the given example is based on the entire field winding of the test machine (Paper III and Paper IV). Figure 57 presents three different situations, which help to understand how to determine the needed inductance of the filter, L_F , in order to limit the relative amplitude of the overshoot under 10 % of the DC-link voltage.

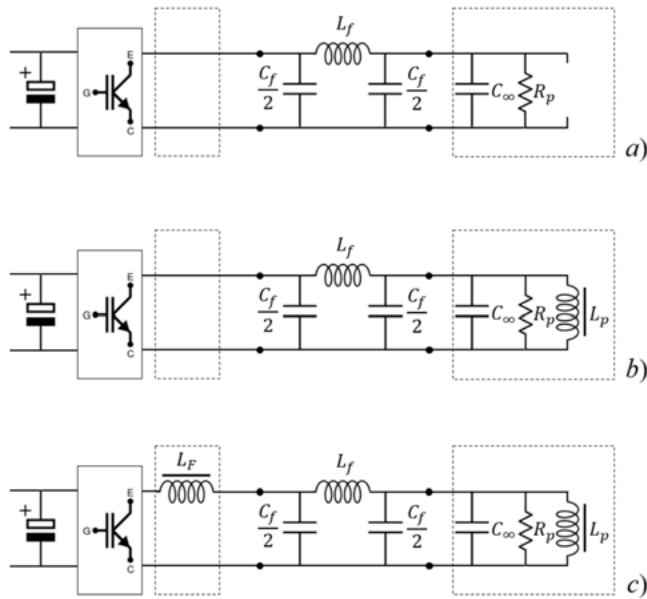


FIGURE 57 – Three test conditions for the design of the low-pass filter: a) supercritical field winding model, b) complete winding model, c) complete winding model with filter.

In all three situations in Fig. 57 the attention focuses on the modulus of the transfer function $F(j\omega)$ given by the ratio of a hypothetical harmonic voltage at the field winding terminals and the relative harmonic voltage at the exit of the PE. In the first schematic, corresponding to the Fig. 57a, the field winding is assumed to be permanently equal to its supercritical model, where the inductive reactance is so high to represent an open circuit. The correspondent transfer function for this case is represented in Figure 58 with the description “without filter, very high inductance”. It can be observed that from 0 Hz up to 200 kHz, the modulus of the transfer function is almost equal to one. The first resonance is set at 1.44 MHz (Paper IV) and the second at 5.2 MHz by the cable.

When the real field winding inductance is included into the model, as represented in Fig. 57b, the transfer function does not change. The correspondent plot in the figure is the one addressed by “without filter, actual inductance”. This first comparison between the two first schematics in Fig. 57 points to the fact that for designing the filter it is possible to consider the supercritical capacitance C_∞ of the field winding only, which corresponds to the geometric mean between C_p and C_s .

Considering the worst case scenario, where the voltage edge to treat is the one corresponding to the step function, the residual voltage in Fig. 50b has the amplitude of the DC-link voltage. Since the harmonics which compose the voltage residual are all supercritical, if an attenuation of 10% at least is granted starting from 95.8 kHz (critical frequency of the winding), the resulting overshoot must be necessarily smaller than the 10% of the original one. Since the filter is a second order filter, it attenuates according to -40 dB/dec. For this reason, the cut-off frequency, f_0 , of the filter must be $(10)^{0.5} \cong \pi$ times smaller than the critical frequency, which corresponds to 30.3 kHz. The inductance of the filter is in general larger than the cable inductance but smaller than the field winding inductance. With reference to Fig. 57a, the inductance of the filter sees the sum of the cable capacitance and field winding capacitance. From the relationship

$$L_F = \frac{1}{(2\pi f_0)^2(C_f + C_\infty)}, \quad (74)$$

the inductance of the filter is finally determined.

In Fig. 58, the plots addressed by “with filter” in the legend refer to the transfer functions which include the filter. Both plots provide the required attenuation at the critical frequency of the winding. The filter with quality factor $Q_F=3$ presents a higher emphasis than the one with $Q_F=1$ close to the cut-off frequency.

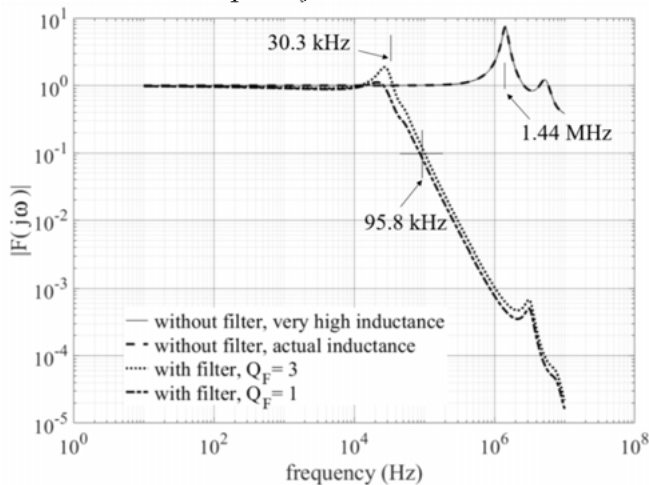


FIGURE 58 – Comparison between different voltage transfer functions.

The dV/dt -filters present in general high quality materials and design in order to minimize the losses and to prevent the overheating. For this reason they are more likely to have higher quality factors than the field winding. Therefore, the maximal attention must be paid for the potential amplification of some specific overtones of the switching frequency, when the quality factor of the filter at the cut-off frequency exceeds the value of 3.

The presented example highlights the importance of the data related to the field winding for performing the design of the filter. In particular the critical frequency and the supercritical capacitance, C_∞ , of the winding are needed, for the determination of which the present work has suggested some experimental procedures.

From Fig. 58 clearly emerges how a low critical frequency of the winding penalizes the available frequency band for the voltage control, since it shifts down the cut-off frequency of the filter. On the other side, a voltage slew rate which is larger than the critical one, which makes the voltage edge steeper than the critical one, requires a stronger attenuation of the filter at the critical frequency. This fact requires as well to set the cut-off frequency of the filter lower and lower. Therefore, it seems that *a compromise between the winding properties (low C_s in order to have high critical frequency but not so low to produce too high relative voltage gradients) and the slew-rate of the PE (as close as possible to the critical slew rate) is the best way to achieve a highly dynamic control of the field current, without producing harmful electric stress for the winding.*

6. Conclusions

The aims of this licentiate thesis have been three: first of all to evaluate if the application of fast switching PE-devices to the field current control in salient pole WFSM is consistent with the risk of producing overvoltages and harmful voltage gradients in the rotor winding. Secondly, to identify the parameters which have an influence on these kind of phenomena. Third, to suggest some guidelines for designing both PE and field winding, so to mitigate or prevent the electric stress in the rotor insulation, which is related to rapid rising voltage edges. Whereas Paper I, Paper II and Paper III have mainly prepared the model for handling the topic, Paper IV has finally addressed the first and the second of the stated aims. High slew rate voltage fronts can definitely produce overvoltages and important voltage gradients in the field winding of salient pole WFSM. Where the current control is performed on each single pole winding or on separate groups of pole windings (split rotor concept), special attention must be paid to the choice of the DC-link voltage level, especially in large and slow SM. On the one side, the voltage level should be as high as possible, in order to provide the needed current dynamic; on the other side, this cannot be as high as to pose the risk of PD in the winding insulation. This risk is made more concrete by the repetitive nature of the voltage stress and by the increasingly performing switches made available by the state of the art of the PE.

In considering and organizing the outcomes of all the Papers from a final point of view, the thesis only could properly address the third and conclusive aim. Paragraph 5.2 shows how some design features of the field winding can help to mitigate the voltage gradients at the field winding during a rapid voltage edge. The same paragraph illustrate the design of an inductive dV/dt -filter starting from two simple data related to the field winding: the winding critical frequency and the supercritical winding capacitance.

Besides, the experimental work has contributed many interesting evidences about the AC-behavior of the field winding. First of all, that the field winding of solid salient pole WFSM appears “electrically shorter” when the rotor is inserted in the stator bore. This fact suggests to perform repetitive high voltage tests on the field winding of a solid salient pole SM, when the rotor is outside the machine bore. It turns out to be the harshest test condition. Moreover, in solid salient pole SM, the AC-resistance of the field winding does not account for eventual eddy currents induced in the stator iron, starting from hundreds of hertz already. Furthermore, the experimental tests have highlighted a strong

negative correlation between the AC field winding inductance and the frequency, because of the eddy currents. This evidence points to the need of laminating the magnetic circuit of the rotor, in all those applications of the WFSM, where a rapid adjustment of the main flux is required. Another important evidence shows that, in a solid salient pole WFSM, the inhomogeneity of the airgap reluctance, due to the stator slotting and/or to the rotor/stator eccentricity and/or ovality, are hardly sensed through the variation of the field winding inductance. Finally, the experimental work has shown that the simplistic theoretical separation between subcritical and supercritical frequencies has a concrete counterpart in the voltage transient phenomena interesting the field winding. In the case of a static ES, where the field winding is supplied by a PE located in a cabinet by means of a more or less long cable, the critical separation of the frequencies helps greatly in conceiving and designing solutions for the “voltage ringing” issue. This kind of approach seems to be a more straightforward approach to that problem than the classic “matching” between the load and the cable characteristic impedance.

7. Future work

This work could be improved by repeating the same set of tests applied to a salient pole WFSM in a round rotor WFSM too. Remaining focused on salient pole SM, a deeper and better look at the internal structure of the multilayer winding could disclose interesting aspects related to the inhomogeneity of the winding properties. Moreover, overvoltages and voltage gradients in the winding has been studied so far with the only reference to a differential mode excitation voltage produced by the PE. It cannot go unnoticed that one terminal of the winding has been permanently kept grounded in the majority of the experimental tests conducted. It would be interesting to study the field winding response in the case of a common mode excitation voltage, which plays an important role in the coordination of the rotor fault protections and in the undesired production of leakage currents through functional (bearings) and structural mechanical parts of the SM. Moreover, the limitation of the drawn conclusions to a solid salient pole WFSM should be definitively removed. This could be done by building a rotor prototype with a laminated magnetic circuit, in order to check: a) the order of the improvement of the quality factor of the winding inductance, especially at high subcritical frequencies; b) the relative importance of both insulation- and Joule losses of the winding with respect to the eddy current losses; c) the effects of the rotor magnetic circuit lamination on the correlation between the magnetizing inductance of the field winding and the frequency.

The construction of a laminated rotor is already ongoing, in order to achieve a faster flux control in the studied test synchronous machine. In this case, the two targeted applications are directly related to the AC-current injection in the field winding and make use of MOSFET based fast switching PE. The first application concerns the start of the SM as a doubly fed asynchronous machine, with the aim to obtain a non-pulsating starting torque. The second application aims to provide the active damping of the rotor oscillations by surrogating the function of the damper bars. Finally, once the rapid control of the flux in the machine has been made possible by the special rotor design and by the PE, many other specific tests on the SM can be envisaged, such as stability tests, fault or low-voltage ride-through tests, short circuits tests.

8. Summary of papers

This chapter summarizes the content of the four paper on which this thesis is based upon and describes the author contribution to each paper.

Paper I

Experimentally validated model of a fast switched salient pole rotor winding

In this paper the demagnetizing effect of the eddy currents in the rotor and stator iron is related to the change of the field winding inductance of a solid salient pole synchronous machine. A Single Transmission Line Model for the field winding of the same machine is proposed for the first time. Two experimental methods are presented for determining the field winding inductance (here considered constant) and the parasitic capacitances.

The author built the model, designed and performed the experimental work, carried out the simulation, validated the data and wrote the paper.

Presented by the author at the 4th IEEE Workshop on Electrical Machines Design, Control and Diagnosis, Athens, Greece, WEMDCD 2019.

Paper II

The influence of eddy currents on the excitation winding impedance of solid and laminated salient pole synchronous machines

This paper provides a rational explanation of the parameters which influence the AC-inductance and resistance of the field winding. It proves that the electrical model of the field winding with a parallel resistance is the most suitable, among the simplest models, in order to account for the eddy current losses.

The author built the model, performed the experimental work, carried out the simulation, validated the data and wrote the paper.

Published in *Electr Eng*, 102, (2553–2566), 2020.

Paper III

An experimentally determined field winding model with frequency dependent parameters

This paper presents the experimental setups for determining the STLM parameters, which reproduce the field winding behavior during the simulations. The experimental work offers an insight into the dependence of the parameters on

the frequency. The results obtained for the winding voltage distribution simulation at different frequencies match with the measured ones and point to the preferable use of the STLM in the frequency domain.

The author built the model, designed and performed the experimental work, carried out the simulation validated the data and wrote the paper.

Accepted for publication in *IET Electric Power Applications*, 2021.

Paper IV

Simulation of rapid edge related voltage surges in highly inductive windings with frequency dependent parameters

This paper proves the suitability of the model prepared in Paper III for performing the simulation of voltage surges in the field winding, which are produced by rapid voltage fronts. The excitation of the winding by fast voltage edges is completely handled in the frequency domain. The voltage responses are finally F-inverse-transformed, back to the time domain. The paper shows the importance of knowing the critical frequency of the field winding in order to avoid the ringing at its terminal, when the excitation winding is supplied by means of a long cable or busbars.

The author performed the experimental work, carried out the simulation, validated the data and wrote the paper.

Manuscript ready to be submitted to a journal during 2021.

9. Svensk sammanfattning

Synkrona generatorer tillgodoser mer än 95% av elbehovet över hela världen. Deras användning i elproduktion beror på att det är lätt att reglera spänningen, genom att helt enkelt justera likströmintensiteten i deras rotorlindning. Ändå avslöjar den snabba utvecklingen av kraftelektronik nya möjligheter för växelströmstillägg i en mer än ett sekel lång DC-dominerad teknik. Dämpning av rotorsvängningar med mindre energiförlust än tidigare, minskning av lagerslitage genom att aktivt kompensera den mekaniska obalansen hos de roterande delarna, uppstart av en synkronmotor utan behov av ytterligare medel, detta är bara några av de nya applikationerna vilka antyder partiell eller total växelströmstillförsel till rotorlindningen. Denna avhandling undersöker vad som händer i en lindning som traditionellt utformats för likströmstillförsel när den drivs med växelström från en växelriktare. Forskningen fokuserar på synkronmaskiner och undersöker förändringarna i fältlindningsparametrarna under växelströmsförhållanden. Särskild uppmärksamhet ägnas åt de potentiellt skadliga spänningsöversvågningar och spänningsgradienterna som utlöses av höga derivata på spänningen. Genom studien har en bredbandsförenklad elektromagnetisk modell av fältlindningen tagits fram och validerats experimentellt. Inom den specifika tillämpningen av den snabba fältströmstyrningen ger forskningen några referenser för utformningen av rotormagnetkretsen och för fältlindningen. Slutligen ägnas vissa överväganden åt samordningen mellan kraftelektroniken och lindningen.

10. Acknowledgments

I want to name here the Hydroflex Project with gratitude, for having made my research possible, through the funding of the European Union research and innovation programme Horizon 2020, under grant agreement No 764011.

I wish to thank my supervisor Urban Lundin for his valuable help and advice. Thanks to him for always accommodating a time slot for me between his many occupations.

Thanks to Mats Leijon for having allowed me to join the Division of Electricity as a PhD student. Thank you to all the colleagues of the Hydropower Group for their closeness, especially to Johan and Jose.

I wish to thank some colleagues in particular for specific reasons:

- Markus Gabrysch, for having mentored me about “Studentportalen”, to all advantage of the Power Electronics I students.
- Saman Majdi, for his fundamental support in the practical labs.
- Marcus Berg, for the interesting conversations without boundaries.
- Sandra Eriksson, for supervising the procedural development of my PhD program.
- Thomas Götschl, for his technical IT support, which can reach you literally everywhere.
- Per-Richard Lindgren, for answering with patience all my questions about RainDance, circulation of the invoices and super cars.
- Ingrid Ringård and Linn Eriksson, for their joyful and friendly way to guide students through the academic bureaucratic procedures.
- Dana Salar, for being always willing to help with practical aspects related to the work in the hall.
- Per Norrlund, for sharing so nicely and interestingly our common work-space at Ångström, at least until the Covid-19 outbreak.

Thanks to Marianna Giassi, Saman Majdi, Eirini Katsidoniotaki, Victor Mendoza and Anar Ibrayeva for sharing their free time with me.

Thanks to all the colleagues at the Division of Electricity for making the working environment so agreeable and inspiring.

Last but not least, thanks to William and Ilaria for their patience and love, which gifted me with extra time for my studies.

References

- [1] Electricity production worldwide from 2010 till 2018, EIA source, <https://www.eia.gov/international/overview/world>.
- [2] Neidhofer, G.: “The evolution of the synchronous machine,” *Engineering Science and Education Journal*, pp. 239-248, October 1992.
- [3] Hooshyar, H., Savaghebi, M. and Vahedi, A.: “Synchronous generator: past, present and future”, *AFRICON 2007, Windhoek*, pp. 1-7, 2007.
- [4] Nøland, J. K., Nuzzo, S., Tassarolo, A. *et al.*: “Excitation System Technologies for Wound-Field Synchronous Machines: Survey of Solutions and Evolving Trends”, *IEEE Access*, vol. 7, pp. 109699-109718, 2019.
- [5] Croft, T.: *Electrical Machinery*, McGraw-Hill, p. 230, 1917.
- [6] Joho, R.: “Static exciter system for a generator and method of operation”, U.S. Patent 8 008 895 B2, Aug. 30, 2011.
- [7] Chen, Z., Mao, C., Wang, D. *et al.* : “Design and implementation of voltage source converter excitation system to improve power system stability”, *IEEE Trans. Ind. Appl.*, vol. 52, (4), pp. 2778–2788, 2016.
- [8] Nøland, J.K., Lundin, U.: “Step time response evaluation of different synchronous generator excitation systems”, *IEEE International Energy Conference (ENERGYCON)*, Leuven, pp. 1-7, 2016.
- [9] Lin, C. *et al.*: “Self-Excited Synchronous Machine using Airgap Harmonics”, *IEEE Trans. Ind. Electron.*, pp. 1-11, 2020.
- [10] Pérez-Loya, J.J., Abrahamsson, C.J.D., Lundin, U.: ‘Demonstration of active compensation of unbalanced magnetic pull in synchronous machines’, *CSE*, vol.8, pp. 98-107, 2017.
- [11] Pérez-Loya, J.J., Abrahamsson, C.J.D., Evestedt, F. *et al.*: “Demonstration of Synchronous Motor Start by Rotor Polarity Inversion”, *IEEE Trans. Ind. Electron.*, vol. 65, (10), pp. 8271-8273, 2018.
- [12] Hlioui, S., Amara, Y., Hoang, E. *et al.*: “Overview of hybrid excitation synchronous machines technology”, *2013 International Conference on Electrical Engineering and Software Applications*, Hammamet, pp. 1-10, 2013.
- [13] Hu, W., Zhang, X., Yin, H. *et al.*: “Analysis of Magnetic Field and Electromagnetic Performance of a New Hybrid Excitation Synchronous Motor with dual-V type Magnets”, *Energies*, vol. 13, (4), p. 1501, 2020.
- [14] Huang, A. Q. : “Power Semiconductor Devices for Smart Grid and Renewable Energy Systems”, *Proc. IEEE*, vol. 105, (11), pp. 2019-2047, 2017.

- [15] Hameyer, K., Ruf, A. and Pauli, F.: “Influence of fast switching semi-conductors on the winding insulation system of electrical machines”, *IPEC-Niigata 2018 -ECCE Asia*, pp. 740-745, 2018.
- [16] Ruffo, R., Guglielmi, P. and Armando, E.: “Inverter Side RL Filter Precise Design for Motor Overvoltage Mitigation in SiC-Based Drives”, *IEEE Trans. Ind. Electron.*, vol. 67, (2), pp. 863-873, 2020.
- [17] Tran, D., Segond, G. and Dossantos, V. : “Modeling and Analysis of EMI and Overvoltage Phenomenon in SiC Inverter Driven Motor at High Switching Frequency”, *IEEE PEMC-Budapest*, pp. 268-273, 2018.
- [18] Zoeller, C. , Vogelsberger, M. A., Wolbank, T. M et al.: ‘Impact of SiC semiconductors switching transition speed on insulation health state monitoring of traction machines’, *IET Power Electron.*, vol. 9, (15), pp. 2769-2775, 2016.
- [19] IEC 60034-18-41 ed. I, Rotating electrical machines - Part 18-41: Partial discharge free electrical insulation systems (Type I) used in rotating electrical machines fed from voltage converters – Qualification and quality control tests, 2014.
- [20] Arkadiew, W.: “Die Theorie des elektromagnetischen Feldes in ferromagnetischen Metallen und die Berechnungen von R. Gans”, *Ann. Phys.*, vol. 360, pp. 643-656, 1921.
- [21] Dreyfus, L.: “Die Feldverteilung und Wirbelströmbildung in den Ankern von Dynamomaschinen bei Unmagnetisierung durch hochperiodige Wechsel- und Drehfelder, Archiv für Elektrotechnik”, 1915.
- [22] Kaden, H., *Wirbelströme und Abschirmungen in der Nachrichtentechnik*, Springer-Verlag, Berlin, pp. 15-19, 1959.
- [23] Heaviside, O.: “On the extra current”, *The London, Edinburgh, and Dublin Philosophical Magazine and Journal of Science*, vol. 2, (9), pp.135-145, 1876.
- [24] Jiao, C., Xia, Z., Fu, W. N.: “A Generalized Multiconductor Transmission Line Model and Optimized Method for the Solution of the MTL Equations”, *International Journal of Antennas and Propagation*, Hindawi Publishing Corporation, 2012.
- [25] Popović, Z., Popović, B., D.: *Introductory Electromagnetics*, Prentice Hall, Upper Sudden River, NJ, p. 324, 2000.
- [26] Chipman, R. A.: *Theory and Problems of Transmission Lines*, , Schaum’s Outline Series, McGraw-Hill Book Company, New York), p. 49, 1960.
- [27] Popov, M., van der Sluis, L., Smeets, R. P. P. *et al.*: “Analysis of very fast transients in layer-type transformer windings”, *IEEE Transactions on Power Delivery*, vol. 22, pp. 238-247, 2007.
- [28] Wright, M.T., Young, S.J., McLeay, K.: “General theory of fast fronted inter-turn voltage distribution in electrical machine windings”, *IET Proceedings*, vol. 130, Pt. B, No. 4, July 1983.

- [29] Tang, Y. : “Analysis of Steep-Fronted Voltage Distribution and Turn Insulation Failure in Inverter-Fed Form-Wound AC Motors”, *IEEE Trans. Industry Applications*, vol. 34, No. 5, Sept./Oct. 1998.
- [30] Krings, A., Paulsson, G., Sahlén, F. *et al.*: “Experimental Investigation of the Voltage Distribution in Form-Wound Windings of Large AC Machines due to Fast Transients”, *XXII International Conference on Electrical Machines (ICEM), Lausanne*, pp. 1700-1706, 2016.
- [31] Luna López, Z., Gómez, P., Espino-Cortés, F. P., *et al.*: ‘Modeling of Transformer Windings for Fast Transient Studies: Experimental Validation and Performance Comparison’, *IEEE Trans. Power Deliv.*, vol. 32, (4), pp. 1852-1860, 2017.
- [32] Smajic, J., Bucher, M., Franz, T. *et al.*: “Modeling of Frequency Dependent Parameters in Time Domain High Frequency Transformer Simulations”, *Procedia Engineering*, vol. 202, Pages 251-263, 2017.
- [33] Filipović-Grčić, D., Filipović-Grčić, B., Uglešić, I.: “High-Frequency Model of the Power Transformer Based on Frequency-Response Measurements”, *IEEE Trans. Power Deliv.* , vol. 30, (1), pp. 34-42, 2015.
- [34] Gustavsen, B. Vernay, Y.: “Measurement-based frequency-dependent model of a HVDC transformer for electromagnetic transient studies”, *Electr. PowerSyst. Res.*, vol. 180, 2020.
- [35] Manyahi, M.J., Leijon, M., Thottappillil, R.: “Transient response of transformer with XLPE insulation cable winding design”, *International Journal of Electrical Power & Energy Systems*, vol. 27, (1), pp. 69-80, 2005.
- [36] Mugarra, A., Platero, C. A., Martínez, J. A. *et al.*: “Large Salient Pole Synchronous Machines Field Windings Diagnosis by Frequency Response”, *XIII International Conference on Electrical Machines (ICEM), Alexandroupoli*, pp. 1875-1880, 2018.
- [37] Ellingson, S. W.: *Electromagnetics*, VT Publishing, VA, vol. 1, p. 49, 2018.
- [38] Rüdénberg, R.: “Performance of travelling waves in coils and windings”, *AIEE Transactions*, vol. 59, pp. 1031-1045, 1940.
- [39] Ivanov-Smolensky, A.: *Electrical Machines*, Mir Publisher, Moscow, vol. 2, pp. 172-176, 1982.
- [40] Pastura, M., Nuzzo, S., Kohler, M. *et al.*: “Dv/Dt Filtering Techniques for Electric Drives: Review and Challenges”, *IECON 2019 - 45th Annual Conference of the IEEE Industrial Electronics Society*, Lisbon, Portugal, pp. 7088-7093, 2019.

Appendices

A.1 Travelling waves equations

With reference to the circuit in Fig.16, the gradient of the line current is equal to the current drained by the specific capacitance of the winding towards ground according to

$$\frac{\partial(i_l+i_k)}{\partial x} = -c \frac{\partial v}{\partial t} \quad (\text{A.1.1})$$

The displacement current flowing between adjacent turns depends on the derivative of the winding voltage gradient by means of the turn to turn specific elastance, k , according to

$$i_k = \frac{\partial}{\partial t} \left(-\frac{1}{k} \frac{\partial v}{\partial x} \right) = -\frac{1}{k} \frac{\partial^2 v}{\partial x \partial t} \quad (\text{A.1.2})$$

The winding voltage gradient descends from the Faraday's law

$$\frac{\partial v}{\partial x} = -l \frac{\partial i_l}{\partial t} \quad (\text{A.1.3})$$

By substituting (A.1.2) in (A.1.1) and differentiating (A.1.1) with respect to t whereas (A.1.3) with respect to x , the following two equations are obtained

$$\frac{\partial^2 i_l}{\partial x \partial t} - \frac{1}{k} \frac{\partial^4 v}{\partial x^2 \partial t^2} = -c \frac{\partial^2 v}{\partial t^2} \quad (\text{A.1.4})$$

and

$$\frac{\partial^2 v}{\partial x^2} = -l \frac{\partial^2 i_l}{\partial t \partial x} \quad (\text{A.1.5})$$

Gaining the double mixed derivative of the conduction current i_l from (A.1.4) and substituting it in the second member of (A.1.5), irrespectively of the differentiation order, it gives

$$\frac{\partial^2 v}{\partial x^2} - lc \frac{\partial^2 v}{\partial t^2} + \frac{l}{k} \frac{\partial^4 v}{\partial x^2 \partial t^2} = 0 \quad (\text{A.1.6})$$

With analogous procedure it is possible to obtain

$$\frac{\partial^2 i_l}{\partial x^2} - lc \frac{\partial^2 i_l}{\partial t^2} + \frac{l}{k} \frac{\partial^4 i_l}{\partial x^2 \partial t^2} = 0 \quad (\text{A.1.7})$$

Equations (A.1.6) and (A.1.7) are linear differential equations of the fourth degree, homogenous, with constant coefficients, representing the travelling and standing waves established into the winding, for the voltage to ground and the conduction current respectively.

A.2 The propagation speed

With reference to the voltage to ground waves equation (A.1.6), the expression of a sinusoidal progressive travelling wave in the complex space is

$$\bar{v}(x, t) = V e^{j\beta x} e^{-j\omega t}, \quad (\text{A.2.1})$$

which is related to the real function

$$v(x, t) = V \cos(\beta x - \omega t). \quad (\text{A.2.2})$$

By substituting (A.2.1) in (A.1.6) the following cardinal equation is obtained

$$-\beta^2 + lc\omega^2 + \frac{l}{k}\beta^2\omega^2 = 0, \quad (\text{A.2.3})$$

which puts the wave angular frequency ω and the wave number β in relationship through the winding parameters

$$\omega = \frac{1}{\sqrt{\frac{lc}{\beta^2} + \frac{l}{k}}}. \quad (\text{A.2.4})$$

The propagation speed can be determined by the ratio between angular frequency (A.2.4) and wave number

$$u = \frac{\omega}{\beta} = \frac{1}{\sqrt{lc + \beta^2 \frac{l}{k}}} = \frac{u_{TEM}}{\sqrt{1 + \beta^2 \frac{l}{ck}}}, \quad (\text{A.2.5})$$

where

$$u_{TEM} = \frac{1}{\sqrt{lc}} \quad (\text{A.2.6})$$

represents the propagation speed of a transverse electromagnetic wave along a lossless line, having specific inductance, l , and capacitance, c . Considering the case of a voltage standing wave in a field winding having length a , which is earthed at its ending terminal, the wave number for the m -th resonance mode is

$$\beta_m' a = m\pi \rightarrow \beta_m' = \frac{m\pi}{a}. \quad (\text{A.2.7})$$

For the case of a field winding with the ending terminal floating instead, the wave number for the m -th resonance becomes

$$\beta_m'' a = (2m + 1) \frac{\pi}{2} \rightarrow \beta_m'' = \frac{(2m+1)\pi}{2a}. \quad (\text{A.2.8})$$

Substituting (A.2.7) and (A.2.8) in (A.2.5), the natural frequencies of the field winding for the earthed and open-circuited winding ending respectively can be obtained:

$$\omega_m' = \left[lc \left(\frac{a}{m\pi} \right)^2 + \frac{l}{k} \right]^{-1/2} \quad (\text{A.2.9})$$

and

$$\omega_m'' = \left\{ lc \left[\frac{a}{(m+\frac{1}{2})\pi} \right]^2 + \frac{l}{k} \right\}^{-1/2}. \quad (\text{A.2.10})$$

In both (A.2.9) and (A.2.10), it can be recognized that the state of the winding ending terminal does not affect the critical frequency

$$\omega_c = \omega'_{m=\infty} = \omega''_{m=\infty} = \sqrt{\frac{k}{l}}. \quad (\text{A.2.11})$$

From (A.2.5), considering (A.2.7) together with (A.2.9), (A.2.8) and (A.2.10), it is possible to obtain the refractive indices of the winding for the two ending states respectively

$$n'_m = \frac{u_{TEM}}{u'} = \sqrt{1 + m^2 \left(\frac{\pi}{L}\right)^2 \frac{1}{ck}} \quad (\text{A.2.12})$$

and

$$n''_m = \frac{u_{TEM}}{u''} = \sqrt{1 + \left(m + \frac{1}{2}\right)^2 \left(\frac{\pi}{L}\right)^2 \frac{1}{ck}}. \quad (\text{A.2.13})$$

In both cases the refractive index diverges when the order of the mode increases. This proves that the propagation speed in the field winding tends to zero when the frequency approximates, for smaller values, the critical one (A.2.11).

A.3 Poles of the voltage transfer function

With reference to the TF defined by equation (26), since

$$\frac{1}{\sinh z} = 0 \quad (\text{A.3.1})$$

does not admit finite solutions, the numerator and denominator of (26) must be independently accountable for the zeros and the poles of the TF respectively. Therefore, for determining the poles of the TF the following condition is set

$$\sinh \mathbf{K}(\mathbf{s})a = 0, \quad (\text{A.3.2})$$

which admits the solutions

$$\mathbf{K}(\mathbf{s}) = \mp i m \frac{\pi}{a} \rightarrow \mathbf{K}^2(\mathbf{s}) = - \left(m \frac{\pi}{a}\right)^2 \quad (m=1,2,3\dots). \quad (\text{A.3.3})$$

With reference to the model in Fig. 15 and neglecting the wire specific resistance in comparison to the winding specific reactance, the squared value of the propagation constant becomes

$$\mathbf{K}^2(\mathbf{s}) = \mathbf{z}(\mathbf{s})\mathbf{y}(\mathbf{s}) = \frac{l\mathbf{s}}{\frac{l}{k}\mathbf{s}^2 + \frac{l}{r_p}\mathbf{s} + 1} (g + c\mathbf{s}) \quad (\text{A.3.4})$$

By substituting (A.3.4) in the second equation of (A.3.3), the following equation in \mathbf{s} is obtained

$$\left[lc \left(\frac{a}{m\pi}\right)^2 + \frac{l}{k}\right] \mathbf{s}^2 + \left[\frac{l}{r_p} + gl \left(\frac{a}{m\pi}\right)^2\right] \mathbf{s} + 1 = 0, \quad (\text{A.3.5})$$

where r_p and l depends on the frequency.

In the last equation, the coefficient of \mathbf{s}^2 is the reciprocal of the square value of the generic natural frequency (A.2.9). Moreover, setting the m -th damping coefficient of the winding as

$$\zeta_m = \frac{\omega_m}{2} \left[\frac{l}{r} + gl \left(\frac{a}{m\pi}\right)^2 \right], \quad (\text{A.3.6})$$

equation (A.3.5) can be rewritten as

$$\frac{1}{\omega_m^2} \mathbf{s}^2 + 2\zeta_m \omega_m \mathbf{s} + 1 = 0. \quad (\text{A.3.7})$$

The solutions of (A.3.7) are the poles of the TF (26) and can be expressed as

$$\mathbf{s}_m = \sigma_m \pm i\omega_{r,m} = -\zeta_m \omega_m \pm i\omega_{r,m} \quad (\text{A.3.8})$$

where

$$\omega_{r,m} = \omega_m \sqrt{1 - \zeta_m^2} \quad (\text{A.3.9})$$

represents the m -th resonance frequency of the winding.

Since the resonance is possible if and only if $0 \leq \zeta_m < 1$, from (A.3.9) descends that the resonance frequency can never be larger than the corresponding natural frequency.

A.4 The winding voltage gradients

With reference to Fig.18 and to (26), the gradient of the specific voltage at the beginning of the line is

$$\frac{1}{V} \frac{dV}{dx} \Big|_{x=0} = -\|\bar{K} \coth(\bar{K}a)\|. \quad (\text{A.4.1})$$

For very high frequency the propagation constant is determined by the parasitic capacitances of the winding essentially, so that

$$\bar{K}_\infty = \sqrt{kC} = \frac{1}{a} \sqrt{\frac{C_p}{C_s}}. \quad (\text{A.4.2})$$

Since the practical values of the ratio between C_p and C_s range between 25 and 100 [39] the

$$\coth(\bar{K}_\infty a) = \coth(5 \div 10) \cong 1 \quad (\text{A.4.3})$$

so that

$$\frac{1}{V} \frac{dV}{dx} \Big|_{x=0} \cong -\frac{1}{a} \sqrt{\frac{C_p}{C_s}}. \quad (\text{A.4.4})$$

A.5 The natural frequencies and the inductance law

The generic natural frequency, f_m , can be found from (A.2.9)

$$f_m = \frac{1}{2\pi} \left[lc \left(\frac{a}{m\pi} \right)^2 + \frac{l}{k} \right]^{-\frac{1}{2}}. \quad (\text{A.5.1})$$

Considering that

$$l = \frac{L_p}{a}, c = \frac{C_p}{a} \text{ and } k = \frac{1}{C_s a}, \quad (\text{A.5.2})$$

(A.5.1) becomes

$$f_m = \frac{1}{2\pi\sqrt{L_p}} \left[C_p \left(\frac{1}{m\pi} \right)^2 + C_s \right]^{-\frac{1}{2}}. \quad (\text{A.5.3})$$

Taking into account the l -st and the m -th natural frequencies of the winding, f_1 and f_m , with $m > 1$, these must both satisfy (A.5.1), so that

$$\begin{cases} f_1 = \frac{1}{2\pi\sqrt{L_p(f_1)}} \left[C_p \left(\frac{1}{\pi} \right)^2 + C_s \right]^{-\frac{1}{2}} \\ f_m = \frac{1}{2\pi\sqrt{L_p(f_m)}} \left[C_p \left(\frac{1}{m\pi} \right)^2 + C_s \right]^{-\frac{1}{2}}. \end{cases} \quad (\text{A.5.4})$$

Raising the equations in (A.5.4) to the square and solving for C_p and C_s , the following expressions are achieved

$$C_p = \frac{1}{m^2-1} \left[\frac{1}{(f_1)^2 L_p(f_1)} - \frac{1}{(f_m)^2 L_p(f_m)} \right] \quad (\text{A.5.5})$$

and

$$C_s = \frac{1}{(m^2-1)\pi^2} \left[\frac{1}{(f_m)^2 L_p(f_m)} - \frac{1}{(mf_1)^2 L_p(f_1)} \right]. \quad (\text{A.5.6})$$

For $m=2$, (A.5.5) and (A.5.6) become

$$C_p = \frac{1}{3} \left[\frac{1}{(f_1)^2 L_p(f_1)} - \frac{1}{(f_2)^2 L_p(f_2)} \right] \quad (\text{A.5.7})$$

and

$$C_s = \frac{1}{3\pi^2} \left[\frac{1}{(f_2)^2 L_p(f_2)} - \frac{1}{(2f_1)^2 L_p(f_1)} \right]. \quad (\text{A.5.8})$$

